Fall 12-15-2023

Experimental Measurement of Near-field Radiative Heat Transfer Between Two Macroscale Planar Media

Md Shofiqul Islam
University of Maine, md.shofiqul.islam@maine.edu

EXPERIMENTAL MEASUREMENT OF NEAR-FIELD RADIATIVE HEAT TRANSFER BETWEEN TWO MACROSCALE PLANAR MEDIA

By

Md Shofiqul Islam

B.S. Chittagong University of Engineering and Technology, 2017

A THESIS

Submitted in Partial Fulfillment of the

Requirements for the Degree of

Master of Science

(in Mechanical Engineering)

The Graduate School

The University of Maine

December 2023

Advisory Committee:

Sheila Edalatpour, Associate Professor of Mechanical Engineering, Advisor

Bashir Khoda, Associate Professor of Mechanical Engineering

Olivier Putzeys, Senior Lecturer and Undergraduate Coordinator of Mechanical Engineering

EXPERIMENTAL MEASUREMENT OF NEAR-FIELD RADIATIVE HEAT TRANSFER BETWEEN TWO MACROSCALE PLANAR MEDIA

By Md Shofiqul Islam

Thesis Advisor: Dr. Sheila Edalatpour

An Abstract of the Thesis Presented
in Partial Fulfillment of the Requirements for the
Degree of Master of Science
(in Mechanical Engineering)
December 2023

Radiative heat transfer between two media separated by a gap smaller than the wavelength of thermal radiation (10 μm at room temperature) is referred to as near-field RHT. Near-field RHT exceeds the RHT between two blackbodies which is the maximum limit for RHT in the far-field regime (i.e., when the separation gap is much larger than the thermal wavelength). Due to this enhanced heat transfer, near-field RHT has found promising applications, for power enhancement of thermophotovoltaic devices, thermal rectification, localized cooling, and photonic cooling to name only a few. Graphene is an ideal material for near-field RHT applications as it is one of the materials with the largest heat flux and it also can emit surface plasmon polaritons resulting a resonantly enhancement of heat flux.

In this thesis, we implement an experimental setup for measuring far-field and near-field RHT between two macroscopic planar media separated by a nanoscale vacuum gap. The validity of the setup is demonstrated by comparing the measured heat flux data with theoretical predictions. The implemented setup is then used for demonstrating that the near-field RHT between two dissimilar dielectric media can be enhanced by depositing a layer of graphene on one of the media. The outcome of this study is an experimental setup which can be used for measuring the far-field and near-field RHT between arbitrary materials as well as experimental demonstration of the graphene potential for near-field RHT applications.

ACKNOWLEDGEMENTS

First and foremost, I am deeply grateful to my advisor, Dr. Sheila Edalatpour, for her exceptional guidance, unwavering support, and valuable insights throughout the entire research process. Her expertise and encouragement have been instrumental in shaping the direction and quality of this work.

I would like to express my sincere gratitude to Dr. Robert Lad whose support and expertise was vital for my research as he allowed me to work in his lab. In addition, my gratitude extends to Dr. Yingchao Yang who also allowed me to work in his lab. I would also like to express my gratitude to Stephen Abbadessa who helped to develop the coding and experimental setup. I am also grateful to Dr. Bashir Khoda, Dr. Olivier Putzeys who agreed to be part of my thesis committee. I extend my sincere appreciation to my fellow lab mates Saman Zare, Ramin Pouria, Mehran Habibzadeh, and Jahid Hasan Sagor for their valuable feedback and suggestions, technical support, and constructive criticism.

I am indebted to the Department of Mechanical Engineering and the Graduate School at the University of Maine for financial and technical support. My deepest gratitude goes to my family and friends for their unwavering support, love, and encouragement throughout this academic journey. Their belief in me and their constant motivation have been a driving force behind my accomplishments.

TABLE OF CONTENTS

LIST OF TABLES

LIST OF FIGURES

CHAPTER 1

INTRODUCTION

1.1 Near-Field Radiative Heat Transfer

Radiative heat transfer is a process in which energy is exchanged between two bodies through the emission, propagation, and absorption of electromagnetic waves because of temperature difference. The mechanism of radiative heat transfer involves the emission of electromagnetic waves by a hot body, which is then transferred to a colder body through a vacuum or an intermediate medium. The temperature of the emitting object affects the magnitude and the spectrum of radiative heat transfer. Thermal electromagnetic waves, which are produced due to the random movement of charged particles in matter, are emitted by any substance with a temperature greater than absolute zero. The propagating waves can travel into the space to distances more than the thermal wavelength, λ_{max}. This propagating mode of radiation is described by Planck's blackbody distribution which depends on the object's temperature [1]. The evanescent waves are confined to a sub-wavelength distance from the emitting body. When two objects at different temperatures are brought to a sub-wavelength distance from each other, radiative heat flux substantially surpasses the maximum blackbody radiation determined by the Stefan-Boltzmann law. This enhancement is due to the contribution from the evanescent modes (which only exist at subwavelength distances from the emitter) to the heat flux. Radiative heat transfer between bodies separated by a sub-wavelength distance is referred to as near-field radiative heat transfer. The evanescent waves can be emitted in several ways, including the total reflection of propagating waves at the interface between the emitting surface and vacuum, known as frustrated modes. This happens when the angle of incidence of the propagating wave within the emitter exceeds the critical angle, which is determined by the refractive indices of the emitter and interface

materials [2]. Another ways through which the evanescent waves can be emitted are unbound electrons fluctuations and vibrations of transverse optical phonons, which includes surface plasmon-polaritons in metals and surface-phonon-polaritons in dielectrics [3].

Figure 1.1 schematically shows the propagating and evanescent electromagnetic waves at the interface between an emitter and vacuum. Evanescent modes are significant contributors to heat flux when objects are separated by distances ranging from tens to hundreds of nanometers. These modes contribute to a net heat flux that is much greater than what Planck's blackbody theory predicts.

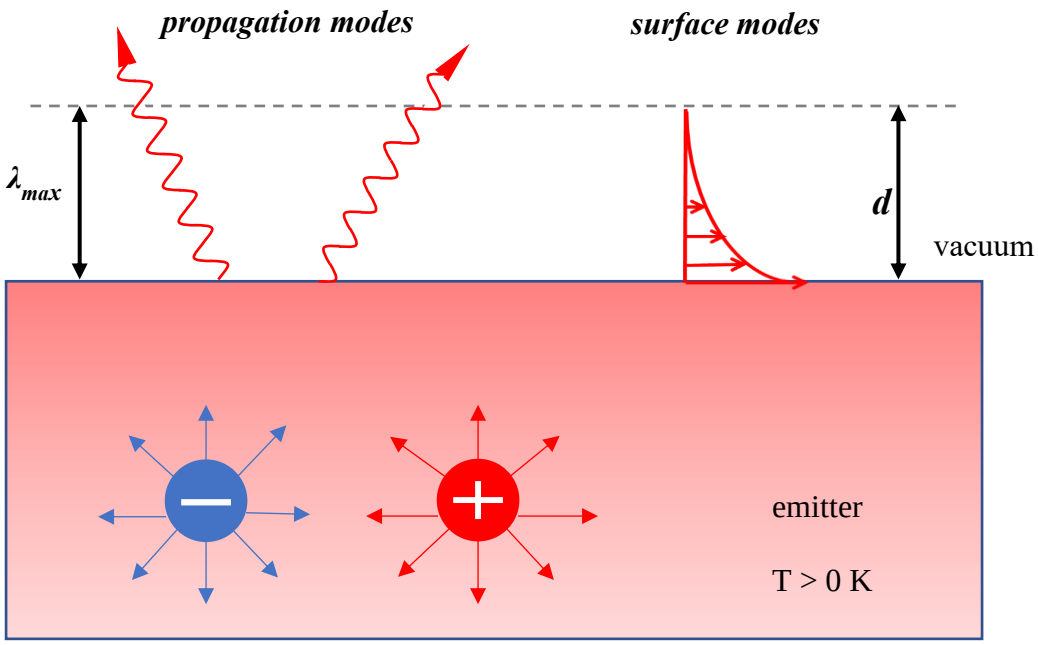

Figure 1.1: Propagating and evanescent electromagnetic waves at the interface of emitting medium and vacuum.

Near-field radiative heat transfer cannot be described by Plank's blackbody theory [4]. since the contribution from evanescent waves existing in the near-field regimes is ignored in the Planck theory. The near-field thermal radiation is described by fluctuational electrodynamics. In this theory, the source of thermal radiation, which is the random motion of charged particles, Is modeled as an stochastic current density, is added to the Maxwells equations [5]. The fluctuating current, which is a result of the thermal agitation of charges inside the emitting object, produces electromagnetic fields that interact with nearby objects. Figure 1.2 illustrates the total heat flux between a SiC emitter and a SiC receiver distanced by a vacuum gap, *d*. The findings reveal a substantial increase in the heat flow as the vacuum distance reduces. Specifically, for a 20-nm vacuum separation, the total radiative heat transfer per unit area (~3×10^5 Wm^{-2}) is 300-fold greater than the maximum blackbody radiation of ~1×10^3 Wm^{-2} and 1000-fold enhancement over the far-field radiation result of ~3×10^2 Wm^{-2}.

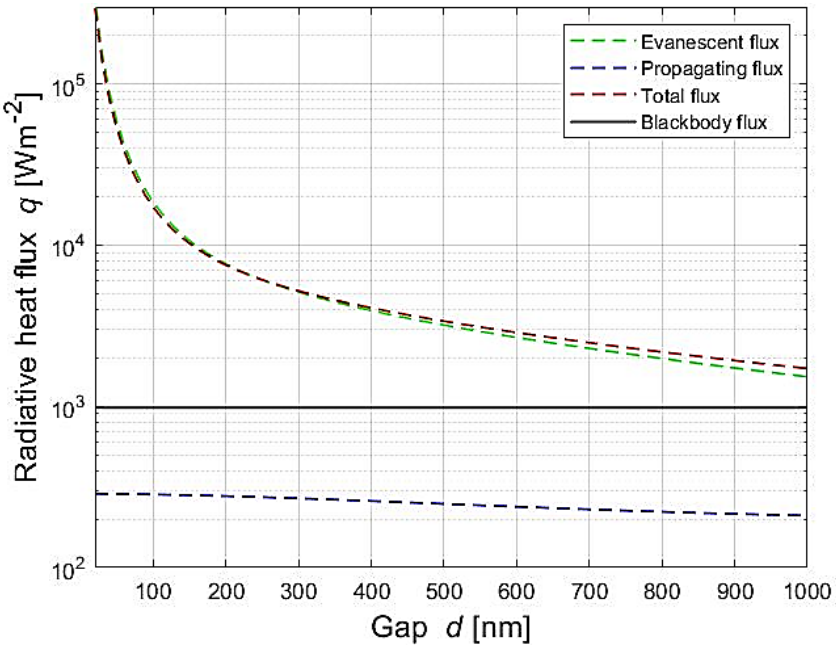

Figure 1.2: The total radiative heat flux (*q*) versus the vacuum gap distance (*d*) is shown for two SiC bulks at temperatures 298 K and 398 K.

According to fluctuational electrodynamics, the thermal radiation is a stochastic process, and the fluctuating currents are assumed to have random amplitudes and phases. These fluctuating currents induce electromagnetic fields which are also stochastic, with random amplitudes and phases [6]. The interaction between these stochastic fields and nearby objects is modeled using the Green's function for Maxwell's equations, which describes how electromagnetic fields propagate and interact with objects in space. Fluctuational electrodynamics can also be used for predicting radiative heat transfer between emitting and receiving objects with sizes smaller than or comparable to the thermal wavelength.

Lastly, it should be mentioned that while far-field radiative heat transfer is usually a broadband phenomenon, the near-field heat flux can be quasi-monochromatic, where the heat flux is resonantly large at a single frequency. For example, Figure 1.3 shows the heat flux versus angular frequency for two SiC plates separated by a gap of 175 nm. The temperature of the emitting and receiving SiC plates are 500 K and 300 K, respectively. It is seen that the heat flux is dominated by the contribution from an angular frequency of ~1.8×10^{14} rad/s. The resonant heat flux at this frequency is due to thermal emission of a special kind of electromagnetic waves referred to as surface phonon polaritons (SPhPs) from SiC.

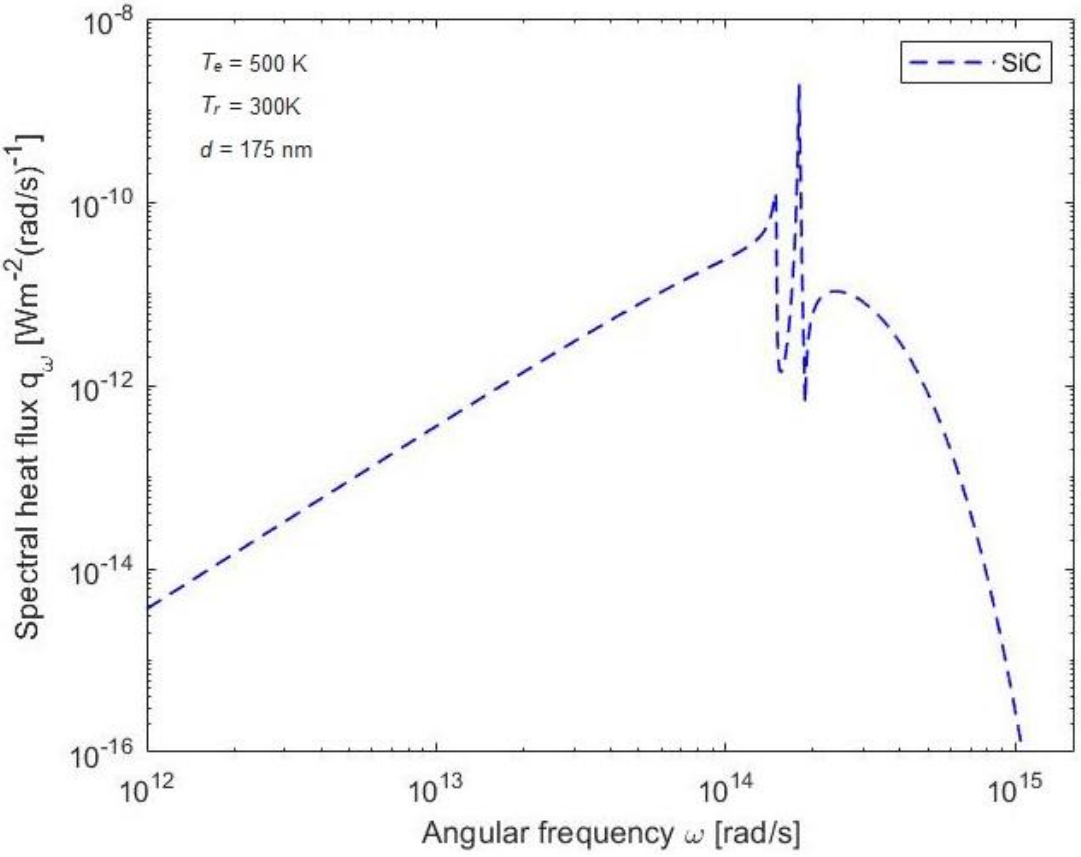

Figure 1.3: The Spectral heat flux q_ω for two SiC plates is plotted versus the angular frequency ω. The graph illustrates how the heat flux varies with respect to angular frequency.

1.2 Applications of Near-Field Thermal Radiation

Since more than 80% of the world's main energy consumption is attributed to fossil fuels like oil, coal, and natural gas [7], whereas eco-friendly energy sources only contribute less than 1% of it, the world urgently needs a globally sustainable energy source. Cutting-edge nanotechnology-enabled photovoltaic cells and equipment are essential to satisfy the global need for sustainable energy. The efficiency of the photovoltaic cell can be increased by near-field thermal radiation [8]. This improvement can be done in thermophotovoltaic system by capitalizing the advantage of near-field evanescent modes [9], [10]. The studies [11-13] have shown an enhanced radiative heat

flux output in near-field regime by a factor of up to 20 over blackbody radiation. Hargreaves conducted measurement with two optically flat plates coated with chromium at a gap distance as small as 1 μm [15]. The results showed that the radiative heat transfer was 50% more than the blackbody radiation. Polder and van Hove [16] also theoretically demonstrated the near-field radiative heat transfer and showed that the results exceeded blackbody radiation. Most recently, near-field radiative heat transfer achieved localized cooling of nanostructures [17], thermal rectification [18], and it has been used in many other applications such as thermal diodes [19], photonic cooling [20], thermoelectric generators [21], heat assisted magnetic storage [22–24], thermal radiation scanning tunneling microscope [25]. In recent years, the study of near-field radiation has regained interest due to its significance in the development of innovative microscopy techniques such as STM, AFM, and NSOM, microelectromechanical devices and thermophotovoltaic applications. The NFRHT also offers a tool for modulating the thermal characteristics of 2D materials [14]. Moreover, NFRHT can be further enhanced using graphene layers which is very promising for thermal application [26], [27]. Svetovoy *et al.* [28] theoretically demonstrated the NFRHT enhancement in thermophotovoltaic cell using graphene. In addition, Yang *et al.* [29], Messina *et al.* [30] showed graphene based NFRHT enhancement experimentally.

1.3 Objectives of the Thesis

This thesis aims at experimental demonstration of enhancement of radiative heat transfer in the near-field regime and using graphene to tune the NFRHT between dissimilar dielectric materials, which are essential to energy harvesting and thermal computing applications [11]–[14], [31]–[35]. The enhancement of NFRHT between dissimilar dielectric media using a graphene layer is also experimentally demonstrated. The possibility of tunning the near-field radiative heat transfer between dissimilar dielectric media has not been explored experimentally so far. The near-field

radiative heat transfer between dissimilar dielectric materials is small due to the mismatch of the resonance frequencies of dissimilar materials. Messina *et al.*[36] theoretically predicted that the heat flux between two dissimilar materials can be enhanced by depositing a graphene layer on one of the materials. We experimentally demonstrate this theoretical prediction and analyze the reason for this enhancement. We measure the NFRHT between LiF and SiC with and without having a graphene sheet on the LiF substrate. The experiment results will contribute to the design and optimization of nanoscale devices such as nano-TPV devices. It can assist in developing innovative thermal management strategies and engineering materials with enhanced thermal properties for electronics, photonics, energy conversion, and thermal sensor applications.

CHAPTER 2

THEORETICAL BACKGROUND

2.1 Radiative Heat Transfer: Near-Field versus Far-Field

There are two different regimes of radiative heat transfer, namely near-field and far-field regimes. In the far-field regime, the heat transfer occurs between media separated by a gap much smaller than the dominant wavelength of thermal radiation. Far-field radiative heat transfer is mediated by propagating electromagnetic waves, which can freely propagate through the space and reach far distances from the emitter. Based on the Stefan-Boltzmann law, the far-field radiative heat transfer between two media with a view factor of 1 is given by [4]:

$$Q = \varepsilon_1 \varepsilon_2 \sigma (T_1^4 - T_2^4) A_1 A_2 \quad (2\text{-}1)$$

where Q is the radiative heat flux, ε_1 and ε_2 are the emissivities of the two media, σ is the Stefan-Boltzmann constant, T_1 and T_2 are the temperature of the media in Kelvins, and A_1 and A_2 are the surface areas of the media. This equation describes the rate at which thermal energy is exchanged between the two media due to thermal radiation. The emissivity value, which falls between 0 and 1, indicates the ability of a material to emit far-field thermal radiation. A value of 0 indicates a surface that reflects all radiation, while a value of 1 indicates a surface that perfectly emits thermal radiation as a blackbody does. The wavelength of the peak thermal emission for a blackbody can be found by Wein's displacement law. This law states that the wavelength with maximum radiation intensity, λ_{max}, is inversely proportional to the absolute temperature, T of the blackbody. Mathematically, it can be described as [37]:

$$\lambda_{max} = \frac{\hbar c}{k_B T} \cong 7.6\ [\mu m]\ \left(\frac{300\ [K]}{T}\right) \quad (2\text{-}2)$$

Figure 2.1 shows the peak wavelength of the radiation at which the emissive power is maximum. The shape of the spectrum curve depends on the temperature of the object.

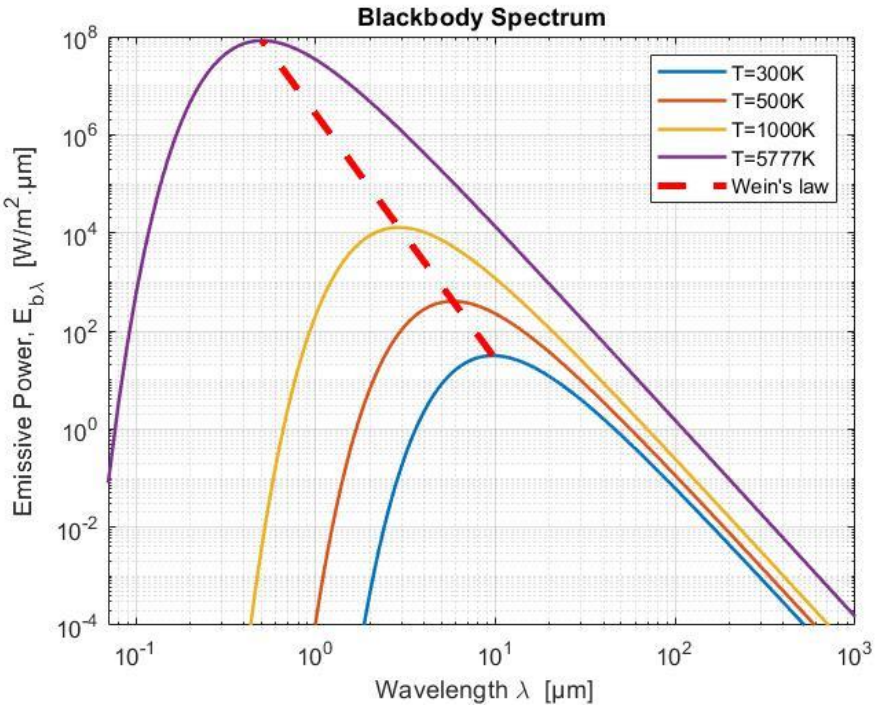

Figure 2.1: The spectrum of the emissive power for a blackbody at various temperatures.

As it can be seen from Figure 2.1, λ_{max} shifts toward shorter wavelengths as temperature increases.

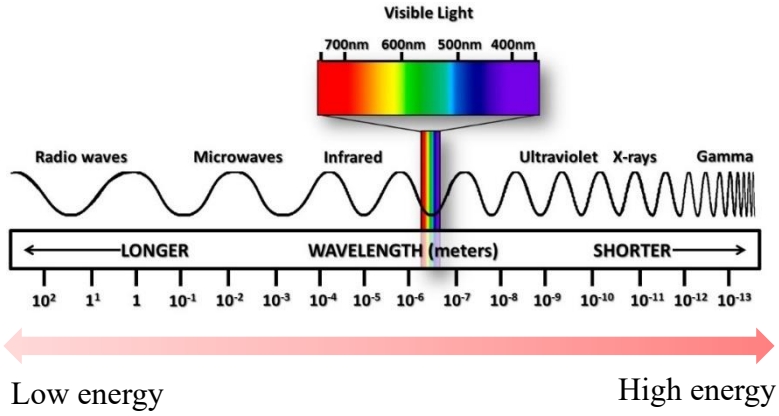

Figure 2.2: Electromagnetic spectrum [38].

The Stefan-Boltzmann law and Wien's displacement law describe the total value of far-field radiative heat transfer and the maximum wavelength of far-field thermal radiation, respectively.

The far-field radiative heat transfer between two bodies is limited to the one between two blackbodies at the same temperature. The Stefan-Boltzmann law is only valid in the far-field regime, where all dimensions are significantly larger than the dominant wavelength of the thermal emission, as is given by the Wein's displacement law.

However, there are two cases where the radiative transfer equation cannot be applied: where the separation distance between the two heat-exchanging media is less than or comparable to λ_{max}, and radiative heat transfer between nanostructures with sub-wavelength dimensions. In these cases, the contribution of easement waves and the size effects on radiative heat transfer are significant. The evanescent waves decay away from the surface exponentially and are due to total internal reflection [39] or thermal emission of surface phonon and surface plasmon polaritons as was described in Section 1.1 and shown in Figure 2-3. When the angle of incidence exceeds the critical angle, the waves can propagate within the slab but not in vacuum, and it is called total internal reflection. These modes are referred to as evanescent modes because they are unable to propagate over long distances in vacuum. Evanescent waves generally contribute to near-field thermal radiation and not to the far-field thermal radiation as they are confined to a sub-wavelength distance from the emitter surface. They are unable to propagate to long distances in vacuum. Surface phonon polariton emitted by (some dielectric media) and surface plasmon polaritons (emitted by some metallic media) are surface waves that are evanescent in both emitting medium and the free space, while they propagate along the interface. Thermal emission of these surface modes, which is due to optical phonons in dielectric media and collective motion of electrons in metallic media, causes a resonance in the spectrum of near-field thermal radiation.

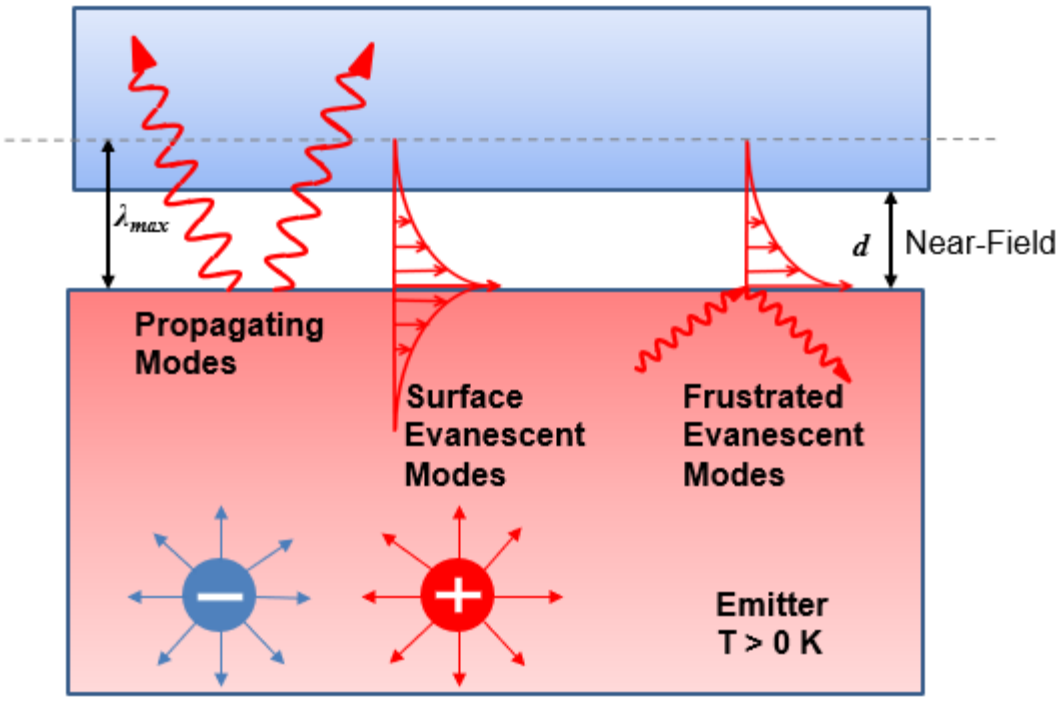

Figure 2.3: Evanescent waves decay away from the surface exponentially.

2.2 Fluctuational Electrodynamics

Near-field radiative heat transfer is described by using a theoretical framework called fluctuational electrodynamics [6]. In this theory, the random motion of the charged particles is modeled as stochastic current density, $\mathbf{J}^{fl}$, which is added to the Maxwell equations as a source term [40]:

$$\boldsymbol{\nabla} \times \mathbf{E} = i\omega\mu\mathbf{H} \tag{2-3}$$

$$\boldsymbol{\nabla} \times \mathbf{H} = -i\omega\varepsilon\mathbf{E} + \mathbf{J}^{fl} \tag{2-4}$$

$$\boldsymbol{\nabla} \cdot (\bar{\varepsilon}\mathbf{E}) = \rho \tag{2-5}$$

$$\boldsymbol{\nabla} \cdot (\mu\mathbf{H}) = 0 \tag{2-6}$$

In Equations 2-3 to 2-6, $\mathbf{E}$ is the electric field, $\mathbf{H}$ is the magnetic field, μ is the magnetic permeability, ε is the permittivity, ω is the angular frequency, ρ is the charge density, and $\mathbf{J}^{fl}$ is

the thermally fluctuating current density. The mean value of the fluctuating current is zero, while its spatial correlation is given by the fluctuation dissipation theorem [40].

$$\langle \mathbf{J}^{fl}(\mathbf{r},\omega)\otimes\mathbf{J}^{fl}(\mathbf{r}',\omega')\rangle = \frac{4\omega\varepsilon_0\varepsilon^{"}}{\pi}\Theta(\omega,T)\delta(\mathbf{r}-\mathbf{r}')\delta(\omega-\omega') \quad (2\text{-}7)$$

where ε_0 is the free space permittivity, $\varepsilon^{"}$ is the imaginary part of the dielectric function of the emitting medium, $\otimes$ indicates the outer product, and $\Theta(\omega,T)$ is the mean energy of an electromagnet state.

The stochastic Maxwells equations presented by Equations 2-4 to 2-7 combined with the boundary conditions should be solved to find the spatial correlations of the electric and magnetic field distributions in the space. Then, the radiative heat transfer can be calculated using the spatial correlations of the electric and magnetic fields.

2.3 Radiative heat flux between two semi-infinite planar media separated by a vacuum gap

For the two planar media separated by a sub-wavelength gap (see Figure 2.4) the stochastic Maxwell equations can be found using the scattering matrix method [41].

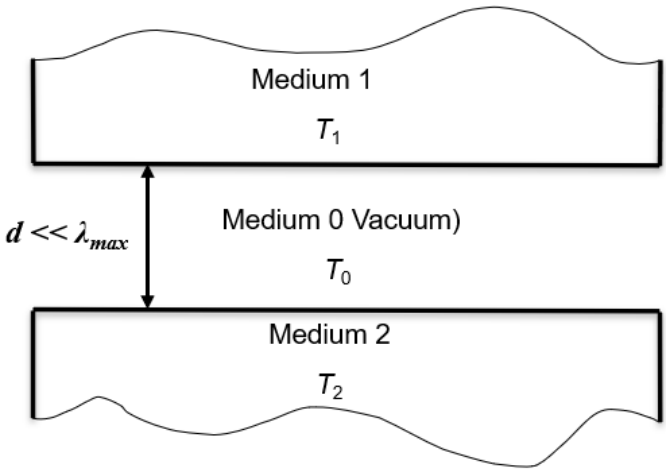

Figure 2.4: Schematic of the system. Two semi-infinite media are separated by a distance *d*.

The net heat flux was calculated as follows. The total heat flux is the sum of contributions from propagating and evanescent waves as:

$$q_{tot} = q^{\text{prop}} + q^{evan} \tag{2-8}$$

where q_{tot} is the total heat flux, and q^{prop} and q^{evan} are the heat flux mediated by propagating and evanescent waves, respectively. The heat flux due to propagating waves, q^{prop}, is given by [42]:

$$q^{prop} = \frac{1}{4\pi^2}\int_0^{\infty} d\omega[\Theta(\omega,T_1) - \Theta(\omega,T_2)]\int_0^{k_0} T_{prop}\, k_\rho dk_\rho \tag{2-9}$$

where $\Theta(\omega,T) = \frac{\hbar\omega}{e^{\hbar\omega/k_BT}-1}$ is the mean energy of an electromagnetic state, k_ρ is the parallel component of the wavevector, k_0 is the magnitude of the wavevector in the free space, and T_{prop} is [42]:

$$T_{prop} = \left[\frac{\left(1-|r_{01}^{TE}|^2\right)\left(1-|r_{02}^{TE}|^2\right)}{\left|1-r_{01}^{TE}r_{02}^{TE}e^{2i\,\mathrm{Ro1}(k_{z0})d}\right|^2} + \frac{\left(1-|r_{01}^{TM}|^2\right)\left(1-|r_{02}^{TM}|^2\right)}{\left|1-r_{01}^{TM}r_{02}^{TM}e^{2i\,\mathrm{Ro2}(k_{z0})d}\right|^2}\right] \tag{2-10}$$

In Eq. 2-5, the subscript 0, 1 and 2, refer to e to the vacuum gap, emitter, and receiver, respectively, r_{ij}^{γ} is the Fresnel reflection coefficient at the interface of media i and j for γ polarization, k_{z0} is the z component of the wavevector in the vacuum gap, R_{01} and R_{02} are the reflection coefficient at the interface of medium 0 and 1, at the interface of medium 0 and 2, respectively. The heat flux due to evanescent waves, q^{evan}, is given by [42]

$$q^{evan} = \frac{1}{\pi^2}\int_0^{\infty} d\omega[\Theta(\omega,T_1) - \Theta(\omega,T_2)]\int_{k_0}^{\infty} T_{evan}\, k_\rho e^{-2\mathrm{Im}\,(k_{z0})d} dk_\rho \tag{2-11}$$

where Im shows the imaginary part of a complex number and

$$T_{evan} = \left[\frac{\mathrm{Im}\,(r_{01}^{TE})\mathrm{Im}\,(r_{02}^{TE})}{\left|1-r_{01}^{TE}r_{02}^{TE}e^{-2\mathrm{Im}\,(k_{z0})d}\right|^2} + \frac{\mathrm{Im}\,(r_{01}^{TM})\mathrm{Im}\,(r_{02}^{TM})}{|1-r_{01}^{TM}r_{02}^{TM}e^{-2\mathrm{Im}\,(k_{z0})d|^2}}\right] \tag{2-12}$$

When a graphene sheet is placed at the interface of one of the media and the free space, the Fresnel coefficients at the interface of media *I* and *j* are as follows:

$$r_{ij}^{\mathrm{TE}} = \frac{k_{iz} - k_{jz} - \omega\mu_0\sigma}{k_{iz} + k_{jz} + \omega\mu_0\sigma} \tag{2-13}$$

$$r_{ij}^{\mathrm{TM}} = \frac{\varepsilon_{r,j}k_{iz} - \varepsilon_{r,i}k_{jz} + \sigma k_{iz}k_{jz}/\varepsilon_0\omega}{\varepsilon_{r,j}k_{iz} + \varepsilon_{r,i}k_{jz} + \sigma k_{iz}k_{jz}/\varepsilon_0\omega} \tag{2-14}$$

Here, σ is the electrical conductivity of the graphene sheet, $\varepsilon_{r,i}$ and $\varepsilon_{r,j}$ are the dielectric function of medium *i* and *j*, and ε_0 is the permittivity of the vacuum space.

We can use Kubo equation to calculate the electrical conductivity of graphene [43].

$$\sigma(\omega, T, \mu_c) = \sigma^{\mathrm{intra}}(\omega, T, \mu_c) + \sigma^{\mathrm{inter}}(\omega, T, \mu_c) \tag{2-15}$$

Here, σ^{intra} and σ^{inter} are the electrical conductivities from intraband and interband transitions respectively, and they are given by [42]:

$$\sigma^{\mathrm{intra}} = \frac{1}{(\gamma - i\omega)} \frac{2q_e^2 k_B T}{\pi\hbar^2} \ln\left(2\cosh\frac{\mu_c}{2k_B T}\right) \tag{2-16}$$

$$\sigma^{\mathrm{inter}} = \frac{q_{el}^2}{4\hbar}\left[Z\left(\frac{\hbar\omega}{2}\right) + i\frac{4\hbar\omega}{\pi}\int_0^\infty \frac{Z(E) - Z\left(\frac{\hbar\omega}{2}\right)}{(\hbar\omega)^2 - 4E^2} dE\right] \tag{2-17}$$

where q_{el} is the electron charge, γ is the dispersion rate of the electrons, and Z is a function described as [42]:

$$Z(x) := \frac{\sinh\left(\frac{x}{k_B T}\right)}{\cosh\left(\frac{\mu_C}{k_B T}\right) + \cosh\left(\frac{x}{k_B T}\right)} \tag{2-18}$$

In the case where a graphene sheet does not exist on the interface, the electrical conductivity, σ, can be set to zero in Equations 2-13 and 2-14 to find the Fresnel reflection coefficients.

CHAPTER 3

LITERATURE REVIEW ON EXPERIMENTAL MEASUREMENT OF NEAR-FIELD RADIATIVE HEAT RANSFER

Radiative heat transfer between flat surfaces separated by subwavelength (micro and nanometer scale gap) can exceed the far-field blackbody radiation as a result of the presence of evanescent waves including the frustrated total internal reflection waves and surface phonon/plasmon polaritons. Surface polaritons results from the interaction between an electromagnetic field and the mechanical oscillation of energy carriers within materials. In metals and doped semiconductors, the combination of free electron collective motion and electromagnetic radiation gives rise to a surface plasmon polaritons (SPPs) [44], [45]. Similar to this, in polar crystals, the interaction between lattice vibrations and an electromagnetic field creates surface phonon polaritons (SPhPs). Surface polaritons propagate along the interface between two surfaces and they decay exponentially perpendicular to the interface in both the emitting medium and the free space.

There is significant progress in nanotechnology, and hence the practical application of radiative heat transfer in near-field region has become very promising. Near-field thermal radiation is now of significance for various applications, including the thermal management of micro-electro-mechanical systems (MEMS) and nano-electro-mechanical systems (NEMS) [31], [46-48]. Experimental NFRHT efforts are reviewed in this chapter based on the mechanism used for maintaining a sub-wavelength gap between the heat exchanging media.

3.1 Using Polystyrene Nanoparticles as a Spacer

Hu *et al.* [11] conducted experimental NFRHT between two parallel glass plates separated by polystyrene particles with a diameter of 1-1.6 μm. The experiment was done in vacuum environment with a pressure of 8.5×10^{-3} Pa. The hot substrate and the cold substrate

temperatures were at 50 ℃ and 24 ℃, respectively. Polystyrene particles were selected due to their low thermal conductivity. Figure 3-1 shows the heat transfer coefficient versus the gap size and the spectral heat flux versus the wavelength obtained theoretically for the glass plates [11]. There are two peaks in the spectrum of heat flux located at 8.7 and 20.2 μm wavelengths which are due to SPP in glass.

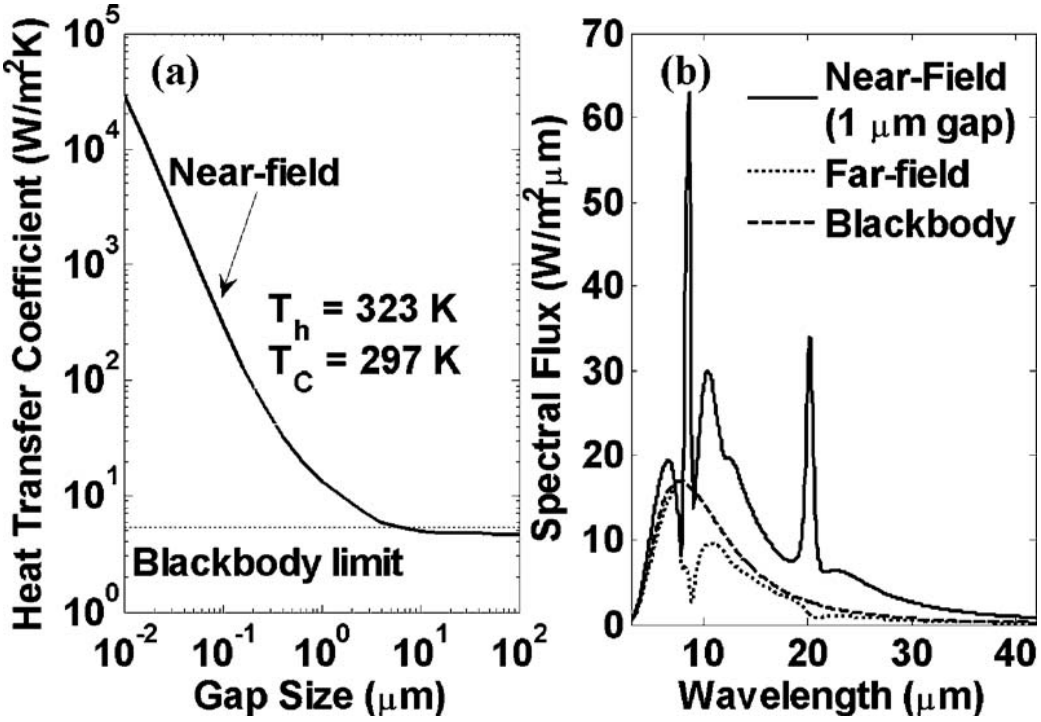

Figure 3.1: (a) Heat transfer coefficient varying with the size of the gap. (b) The spectral radiative heat flux between two glass surfaces determined theoretically [11].

They showed experimentally that at 1 μm gap distance, the near-filed heat transfer coefficient exceeds the blackbody limit by more than 50% over. The experimental setup involved diluting spherical particles in DI water to create a suspension of liquid. Minuscule droplets of the mixture were dispersed on the surface of low temperature side to achieve a homogenous distribution of particles. Approximately 80 particles were deposited between two plates to limit heat conduction.

Once the water particles evaporated, the emitter was positioned above the receiver with the particles acting as spacers. All operations were performed in a dust-free clean room. To test the system, far-field radiation was measured by clamping the emitter to a sample holder with a 2 mm gap between surfaces.

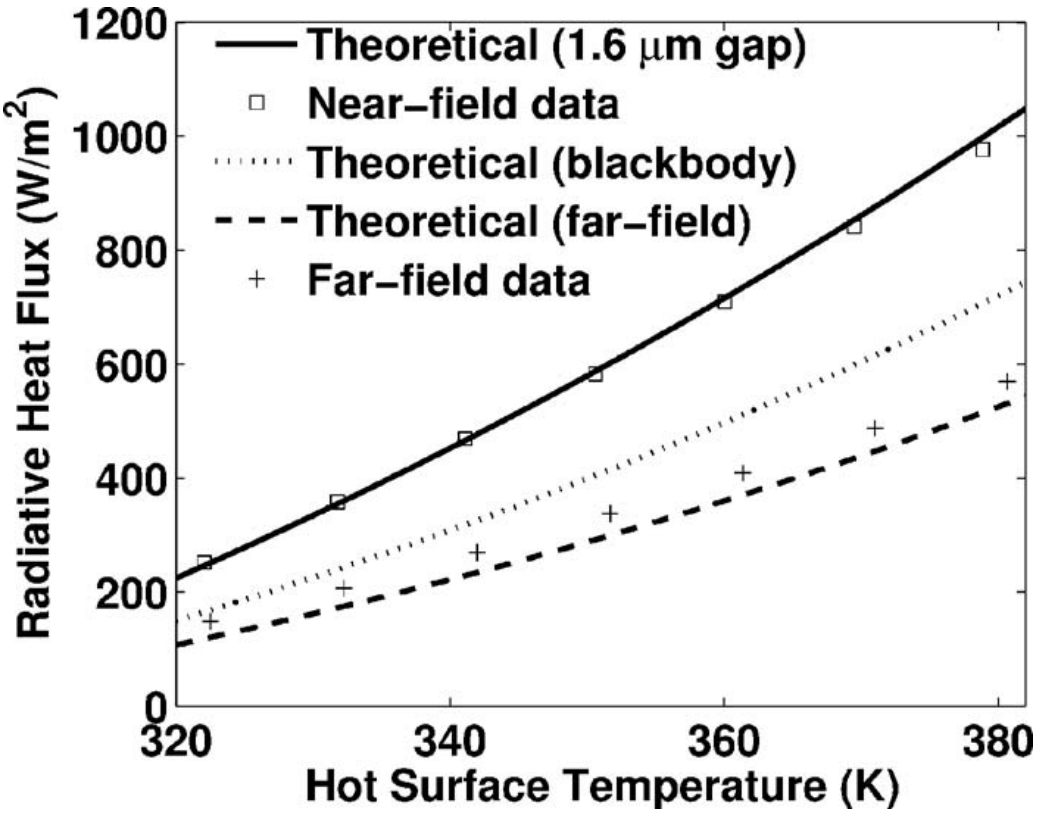

Figure 3.2: Experimental radiative heat flux between two glass substrates [11].

From figure 3-2, the measured radiative heat flux surpasses black-body radiation by over 35% across the entire temperature range. The primary factor contributing to this enhanced heat transfer is the surface phonon polaritons emitted by the glass plates.

Sabbaghi *et al.* [13] also used polystyrene particles in their experiment. The experiment was performed for metallic media made of thin aluminum films with various thicknesses ranging from 80 nm to 13 nm. The thin films were coated on silicon chips as shown in Figure 3-3. The thickness

of the deposited aluminum thin films was measured by an atomic force microscope. Polystyrene particles' nominal diameter was 200 nm, and 0.02 ml of the 7.8×10^6 particles/ml concentration suspension was distributed on the receiver substrate. Temperature difference between the two substrates varied from 25 K to 65 K, and Al thin film thicknesses tested were 13 ± 2 nm, 14 ± 3 nm, 40 ± 3 nm and 79 ± 3 nm.

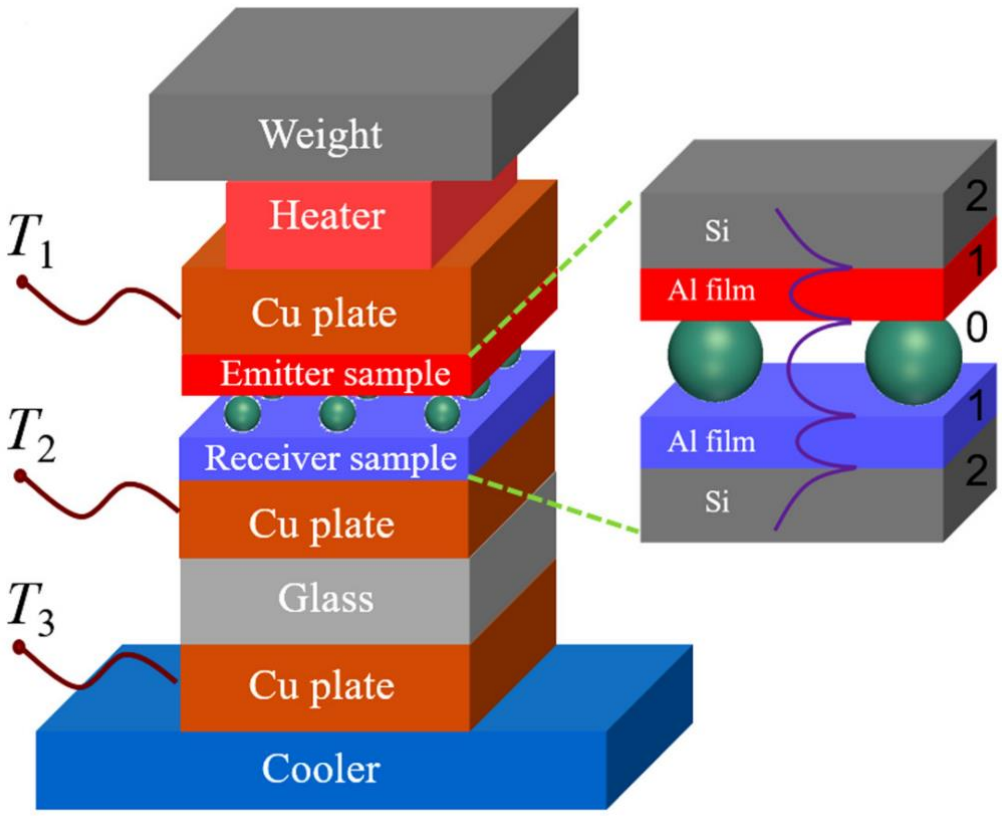

Figure 3.3: Schematic of the experimental setup using polystyrene particles within the Al thin film [13].

They predicted theoretically that a significant enhancement in near-field radiative heat transfer could be achieved with an Al thin film having 5 nm thickness, achieving 11-fold increase compared to the maximum limit of blackbody radiation and 720-fold increase over the far-field limit of

aluminum plates. Further they suggested that with an Al film having 15 nm thickness at a gap distance of 100 nm, the near-field heat transfer amplification could exceed the blackbody limit by 42 times, or by 123 times with an Al film having 20 nm thickness at a gap distance of 50 nm, both with a temperature difference of $\Delta T = 65$ K.

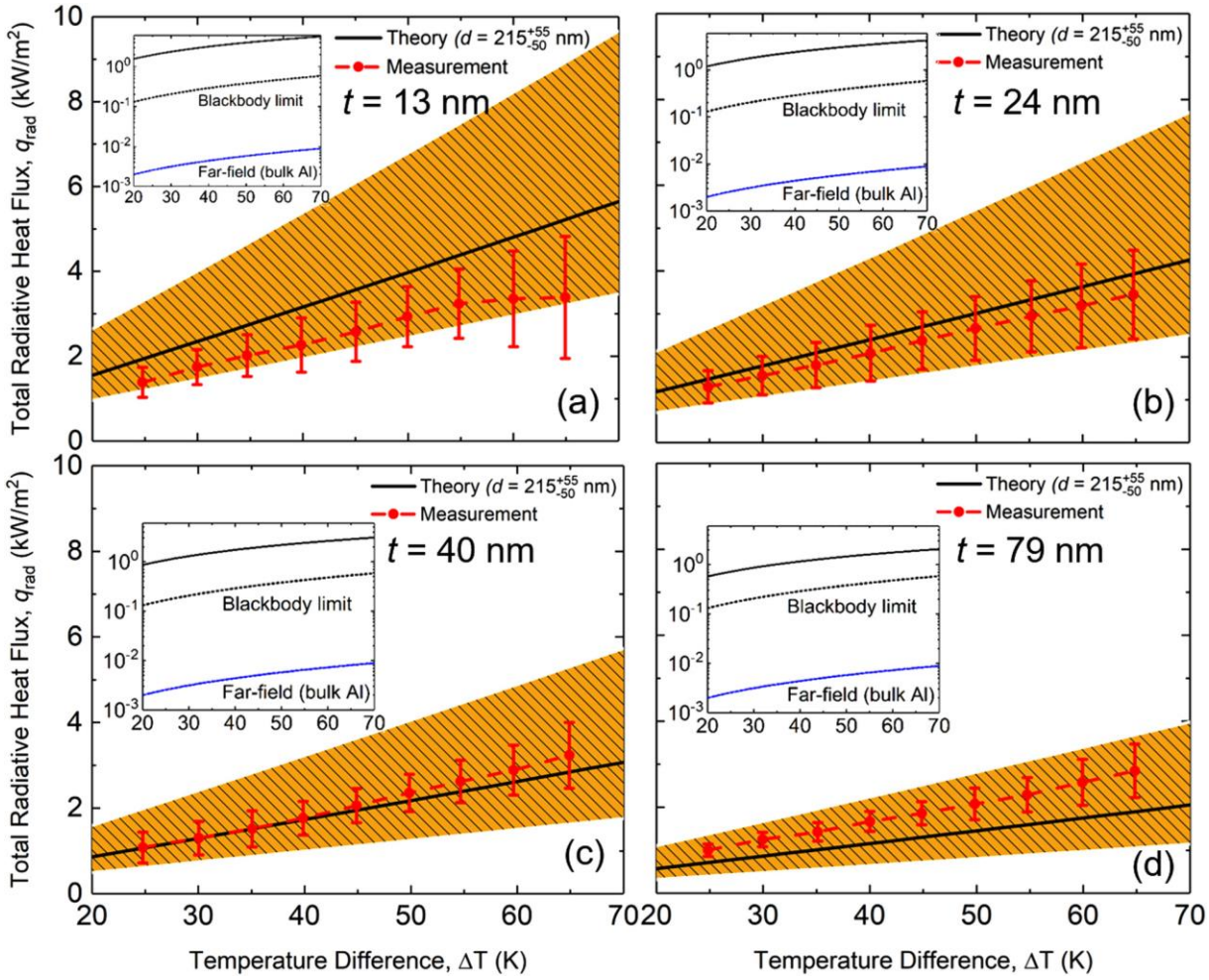

Figure 3.4: The measured near-field radiative heat flux between Al thin films of different thicknesses at various temperature differences (ΔT), in addition to the corresponding theoretical calculation. The markers with error bars represent the experimental data, while the shaded area represents the theoretical calculation at a gap distance of 215 $\pm$ 55 nm using only Si chips. The thicknesses of the aluminum films are (a) 13 $\pm$ 2 nm, (b) 24 $\pm$ 3 nm, (c) 40 $\pm$ 3 nm, and (d) 79 $\pm$ 3 nm. The enclosed small section in the figure compares the total radiative heat flux at a gap

distance of 215 nm with the maximum limit of blackbody radiation and far-field radiative heat transfer limit of aluminum plates.

The measured experimental results show an average of 6.4-fold enhancement over the blackbody radiation and approximately 420-fold enhancement over the far-field radiation, indicating the effectiveness of the thin film in enhancing near-field radiation heat flux.

3.2 Using Nano-Positioner

Ottens *et al.* [49] used an apparatus with stepper motors which can allow adjustment of the gap between two plates, as well as tip and tilt to maintain parallelism. They used two microscopic sapphire plates for radiative experimental investigation of heat transfer under vacuum condition of 2-5$\times 10^{-7}$ Torr range. The gap distance was measured by a capacitance made by depositing a 200-nm-thick layer of sputter copper at each corner. These four coatings at the corners act as capacitor plates which help to adjust the gap and the misalignments. The experiments were conducted for a separation gap varying between 2 and100 μm and a temperature difference in the range of 2.5-30 K.

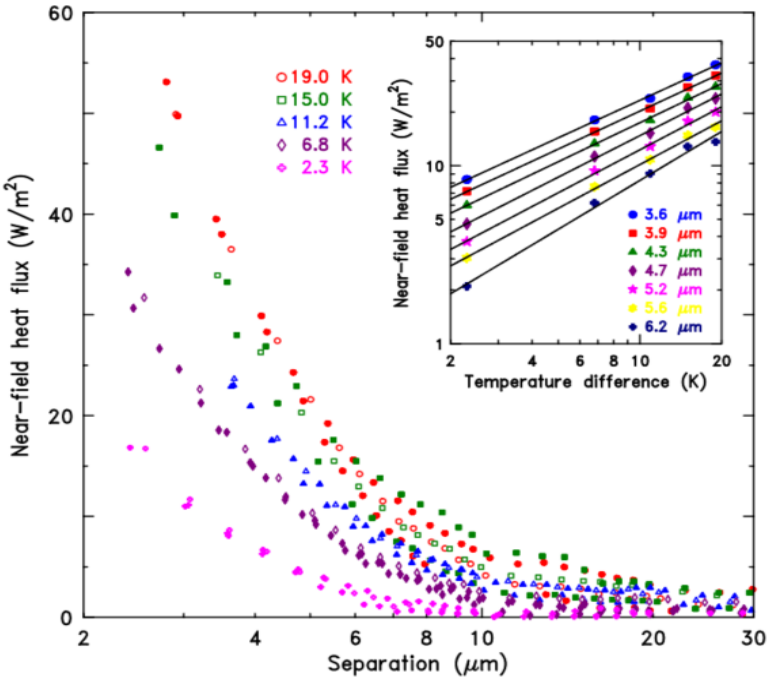

Figure 3.5: Near-Field heat flux versus gap distance for different temperatures [49].

The experimental data showed that the measured heat transfer coefficient of ~ 8.5 W/m^{2}K exceeds the coefficient of ~ 6.7 W/m^{2}K for blackbodies.

Kralik *et al.* [50] demonstrated NFRHT in cryogenic temperatures between metallic and non-metallic plates. They used a mechanical positioning system to maintain parallelism between two plates. The cold plate temperature of ~ 5K was maintained by a liquid helium bath. The experiments were conducted for a separation gap in the range of about 1-500 μm and a temperature difference in the range of 10-40 K [51]. The gap distance was measured using capacitance meter and the accuracy of separation gap was 1 μm.

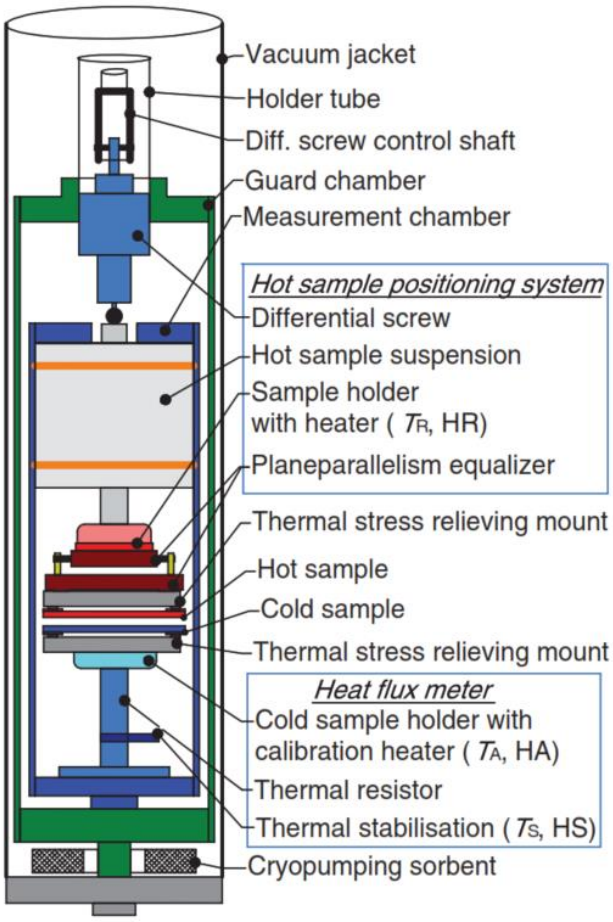

Figure 3.6: Schematic diagram of the main part of the apparatus used for measuring near-field radiative heat transfer in Ref. [50].

The gap between the substrates were maintained using a differential screw. The hot sample was insulated from the rest of the apparatus using a thin-walled tube to prevent conductive heat transfer. The samples were positioned in parallel using a parallelism equalizer that connects the heater and the hot substrate mechanically and thermally. The cold substrate was attached to a heat flux meter and housed in a vacuum jacket measuring 100 cm in length and 48 mm in diameter. At the lower section of the device, there were measurement and guard chambers connected to the apparatus lid through a holder tube. The cold plates holder included a calibration heater, a thin-wall tube acting

as a thermal resistor, a stabilization heater, and two thermal sensors. The measurement chamber, made of 1 mm thick copper, maintained isothermal conditions at the liquid He temperature condition. To minimize the overheating of the sample space, they coated the inside surface of the chamber with a sheet of epoxy composite that absorbs radiation. They achieved a vacuum pressure of 10^{-5} Pa in the chamber.

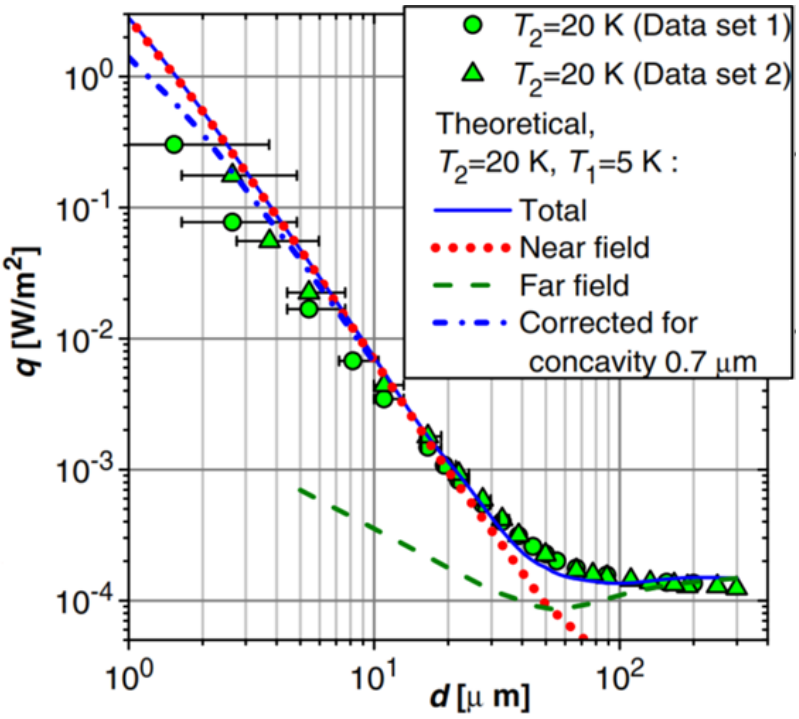

Figure 3.7: Experimental data and theoretical calculation of radiative heat transfer [51].

In Figure 3-7, a significant increase in heat flux between two alumina plates coated with 150 nm of tungsten, reaching levels nearly 10,000 times higher than the expected values in the far-field [42]. This remarkable enhancement is approximately 100-fold greater than the heat flux predicted by Planck's law for two blackbodies.

Ghashami *et al.* [52] measured NFRHT between single crystalline quartz using a Smarpod 110.45 nano positioner. The nano positioner has three piezo-motors, enabling control over the position of

objects in six degrees of freedom in the x, y, and z-directions with translational resolutions as fine as 1 nanometer. Additionally, it provides rotational resolutions of 1 micro-radian along x, y, and z axis. The nano positioner's z-direction has a total travel range of approximately 10 mm, ensuring space for secure sample mounting and pre-alignment procedures.

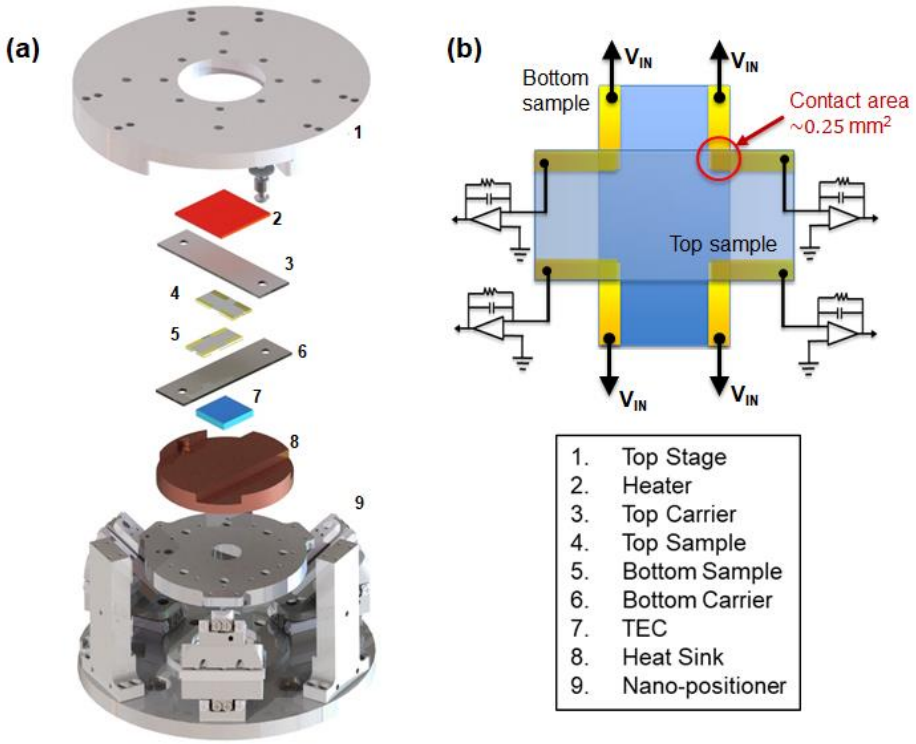

Figure 3.8: (a) Experimental setup used for NFRHT measurement in Ref. [52]. (b) Contact sensors to maintain alignment [52].

In the experiments, temperature gradients varied from 20 K to 160 K and the separation distance changed from 200 nm to 1200 nm in a vacuum pressure of 8×10^{-7} Torr. The cold plate temperature was kept at 301 ± 1 K. A copper heat sink was used to prevent overheating the substrates and a ceramic heater was mounted on the upper surface of the top carrier.

The procedure for achieving parallel gap spacing in the sample is shown in Figures 3-9a-d. Initially, without applying power to the heater and thermoelectric cooler (TEC), the bottom substrate was gently tilted and moved upwards at a slow rate (<10 nm/s) to establish contact at one corner. Then, the bottom substrate was rotated around the x-axis or y-axis until contacts are made in two directions. This rotation step was repeated on the other axis to ensure all four corners make contact. Figure 3-9e demonstrates the usual sensing sequence of the four-corner contact sensors during the sample engagement process. Every signal, represented by a different color, ensures contact between two silver (Ag) pads at a defined corner.

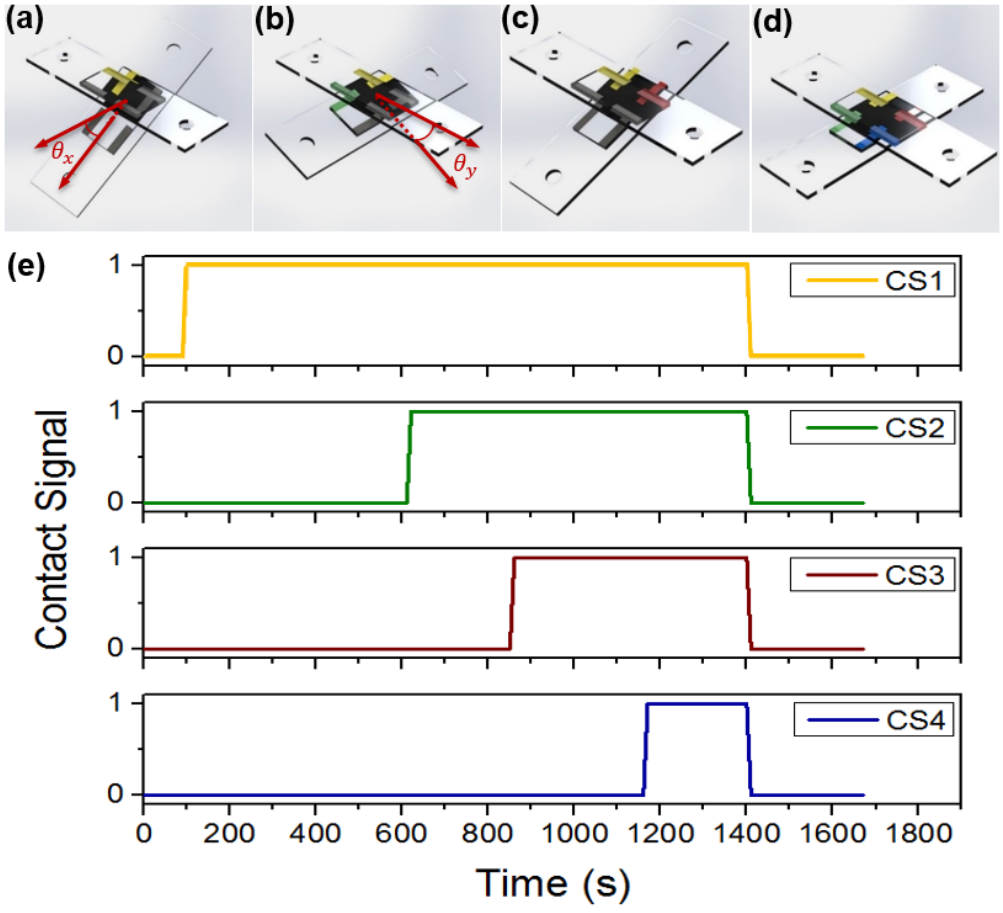

Figure 3.9: The sample engagement process. (a) Initially the bottom plate was tilted and brought close to establish contact at the first corner. (b) The bottom plate was then rotated to make contact at two corners. (c),(d) This procedure was repeated for the other corners until all four

corners can initiate touch. (e) Continuous monitoring of the four contact signals was performed during both the sample connect and disconnect processes [52].

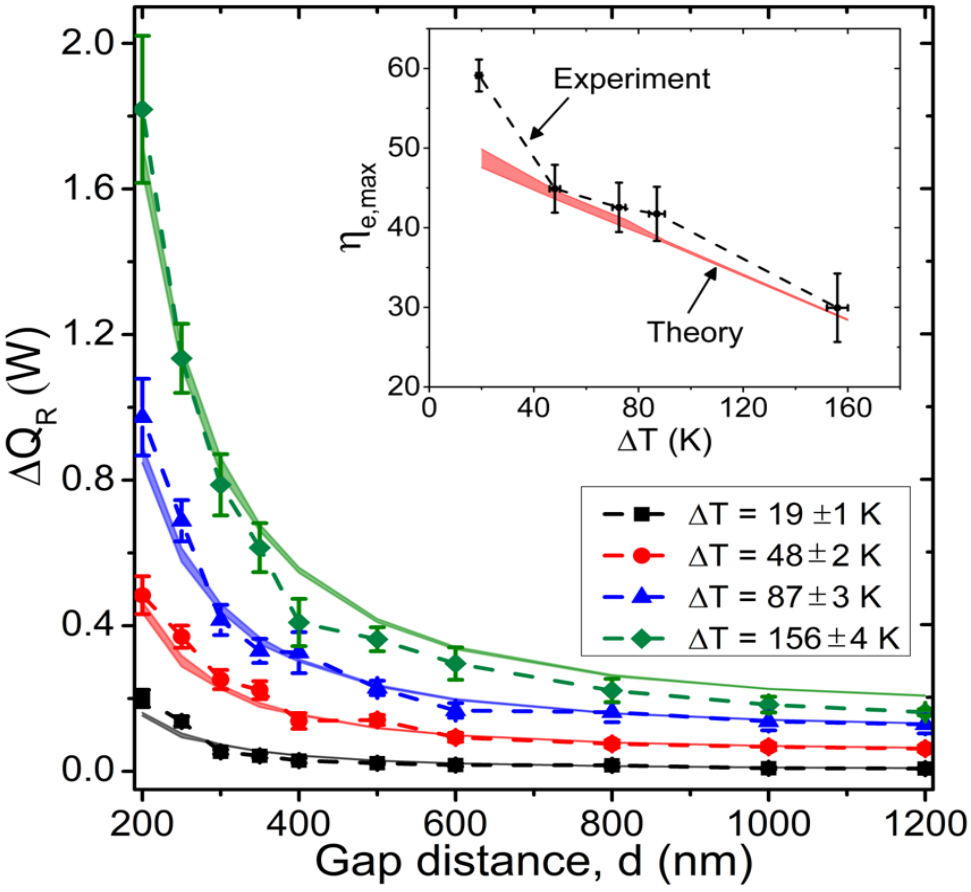

Figure 3.10: Radiative heat transfer in the near-field regime versus gap distance for various temperatures. The inset shows the maximum enhancement factor at a 200 nm gap [52].

Figure 3.10 shows near-field radiative heat transfer for quartz, which is more than 40 times greater than the blackbody radiation limit. This figure illustrates the significant influence of surface phonon polaritons on near field radiative heat transfer.

Song *et al.* [53] built Si-based microdevices to conduct measurements of radiative heat currents between dielectric and metallic plates ($SiO_2 - SiO_2$, Au − Au, SiO_2 – Au and Si – Au surfaces) separated by a nanoscale vacuum gap. The plates have characteristic dimensions of 48 μm × 48 μm and are coated with a desired dielectric (SiO_2) or metal (Au).

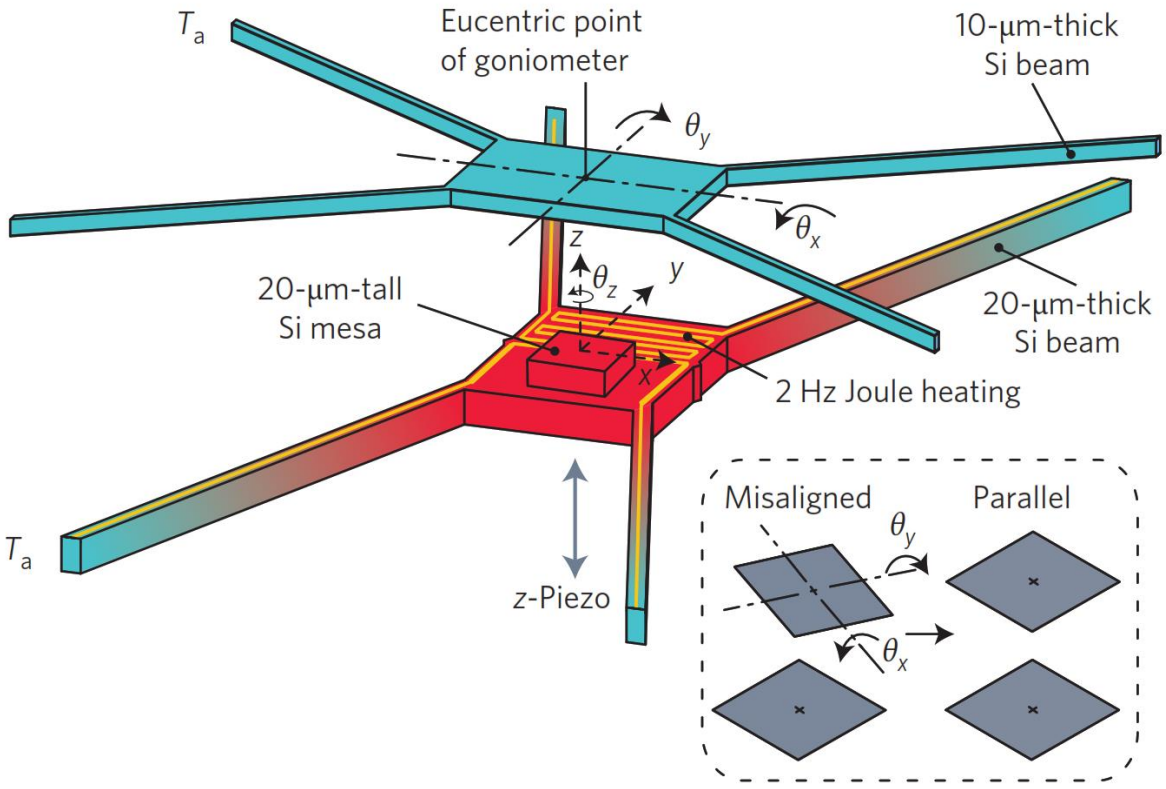

Figure 3.11: Schematic of the relative positions of the emitter and receiver which are maintained by a nano positioner [53].

A custom-designed nano positioner was utilized for the experiment, allowing precise movement in both horizontal and vertical directions. Additionally, the positioner had angular control capability to ensure parallel alignment during the experiment. They studied the radiative heat transfer between emitter and receiver devices which had coating of a 2-μm-thick layer of SiO_2 or

Au and accounted for the inclusion of small particles of up to 30 – 40 nm in size on the microfabricated emitter and receiver surfaces. Figure 3-10 shows the relative orientation of the emitter and receiver devices which were controlled by a piezoelectric actuator.

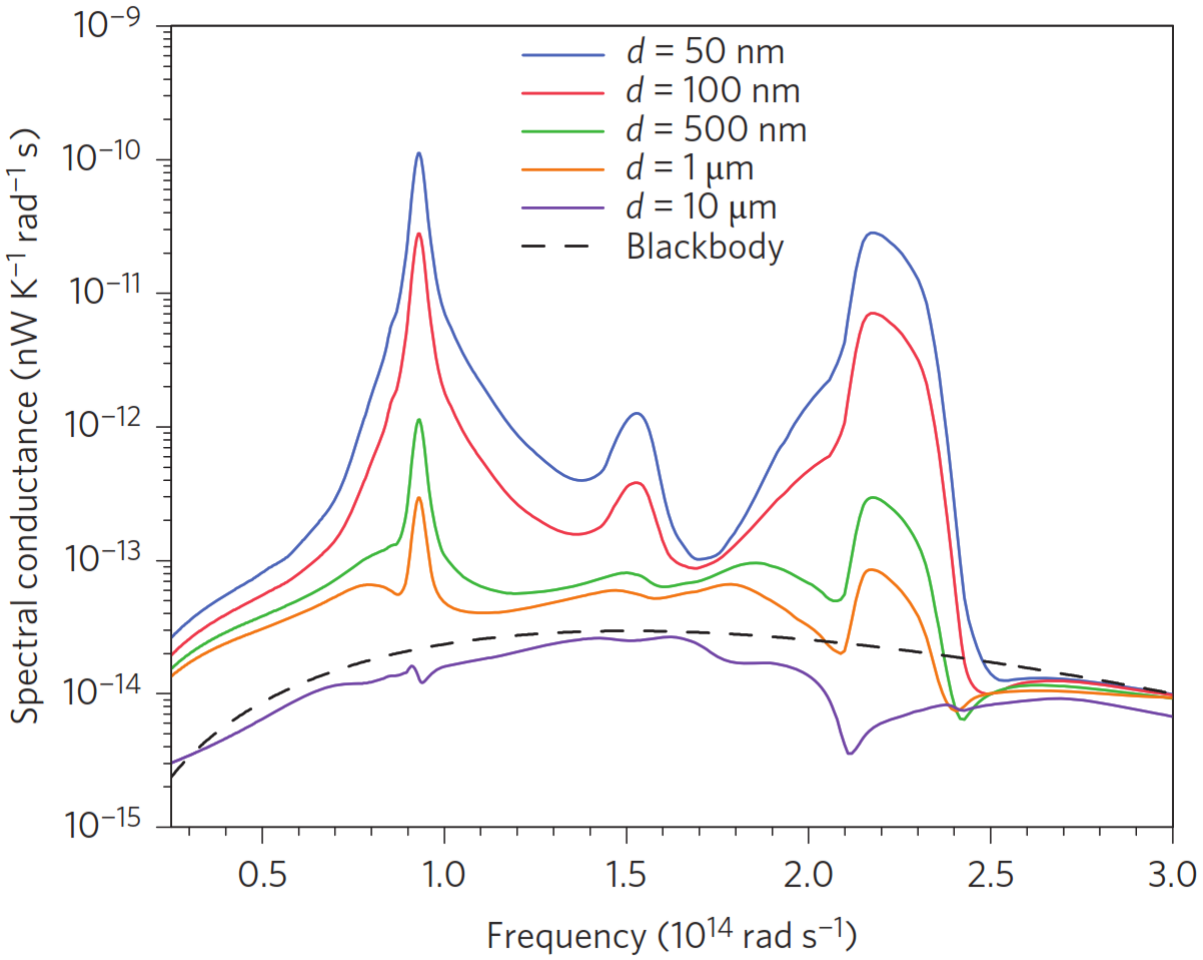

Figure 3.12: Calculated spectral heat conductance for 2-µm-thick SiO_2 film on Si at different gap distances from 50 nm to 10 μm. For comparison, the spectral conductance between blackbodies is also included in the plot [53].

Figure 3-13 shows the measurements between SiO_2 – Au and Si – Au surfaces and the radiative heat transfer enhancement for different dielectric substrates were lower than the surfaces with

similar dielectric properties. Using this technique, they had reported 100 to 1000 times increase of near field thermal radiation above the far field radiation limit. The experimental approach used in this study enables non-contact tunning of thermal conductance and radiative cooling, which could be notable for innovative thermal management strategies.

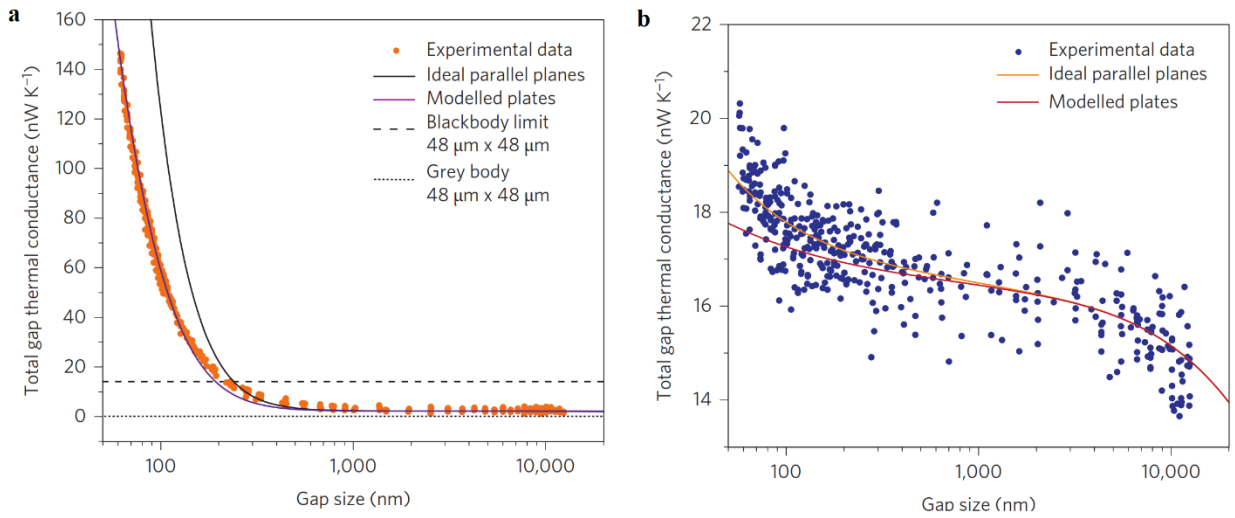

Figure 3.13: (a) The enhanced heat conductance observed between Au surfaces for gaps less than 100 nm. (b) The thermal conductance for mismatched parallel-planar surfaces (SiO2 – Au) at a gap of 55 nm, was measured [53].

3.3 Using Nano Pillars and Microcavities

Kota *et al.* [54] experimented NFRHT by creating nano pillars on a quartz substrate to separate two surfaces. The experiments were conducted for a separation gap range of ~0.5 - 2 μm. They measured the gap size by using optical interferometry at the four corners of the substrate and the a gap under 100 nm between was maintained between the nano pillars. Contact photolithography and wet etching were used to create trapezoidal pillars on the substrate. The separation distance between pillars were 1 mm on a 8.6 × 19 mm^2 substrate.

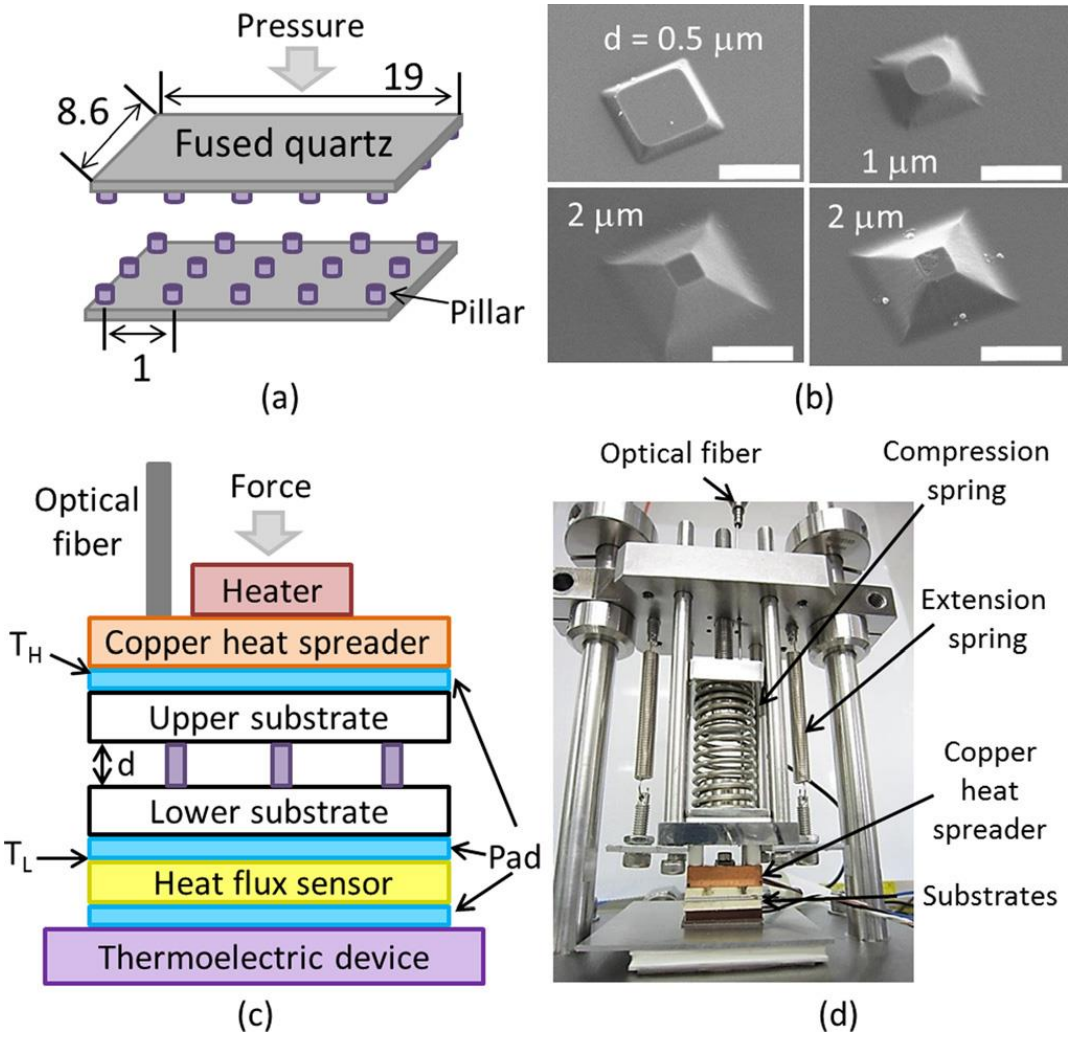

Figure 3.14: (a) A schematic of the nano pillars fabricated on a quartz substrate. (b) SEM images of the fabricated nano pillars. (c) Schematic of the apparatus. (d) Experimental setup [54].

The pressure applied on the substrate was 800 MPa with a compression ring. The vacuum pressure was maintained at 5×10^{-3} Pa. In Figure 3-14, a heat flux meter under the lower substrate was used for measuring the radiative heat flux, and heat was removed from the system through the thermoelectric cooler. The temperature gradients were 5 K, 10 K, 15 K, and 20 K while the lower substrate was maintained at 293 K.

The measured heat flux is shown in Figure 3-15. It is seen from that the measured heat flux is close to the theoretical predictions. The observed deviation is due to the heat conduction through the nano pillars. The conduction heat transfer can be reduced by optimizing the pillar surface area.

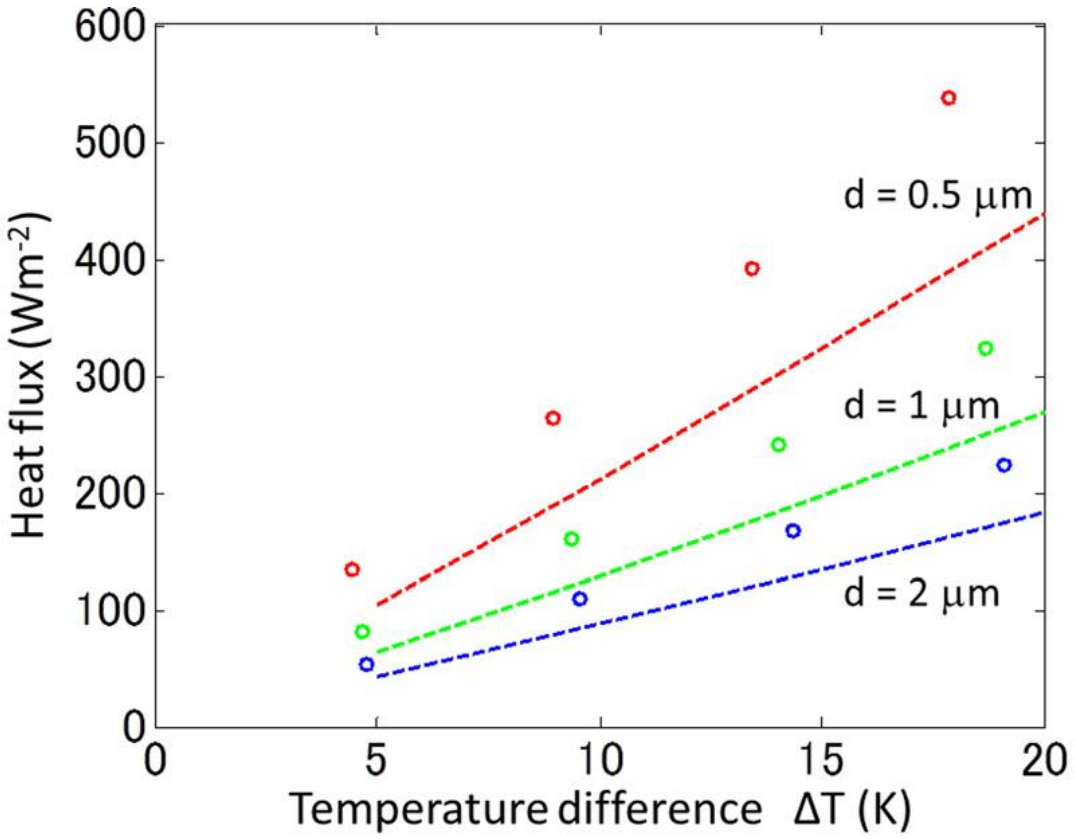

Figure 3.15: Measured heat flux between two fused quartz substrates for different temperature differences. The theoretical predictions are plotted using dashed line, while the circles show the measured heat flux [54].

Ijiro *et al.* [12] conducted NFRHT between SiO_2 plates with and without microcavities. The experiments were conducted at a chamber pressure of $4-5\times10^{-4}$ Pa and a constant chamber temperature of 303 K. The microcavities were created on SiO_2 substrates using electron beam lithography and etching techniques. These microcavities covered an area of 17.5 × 17.5 mm^2,

accounting for 62.4% of the heat-transfer area. The measurements were conducted with a gap-thickness varying from 0.3 μm to 50 μm.

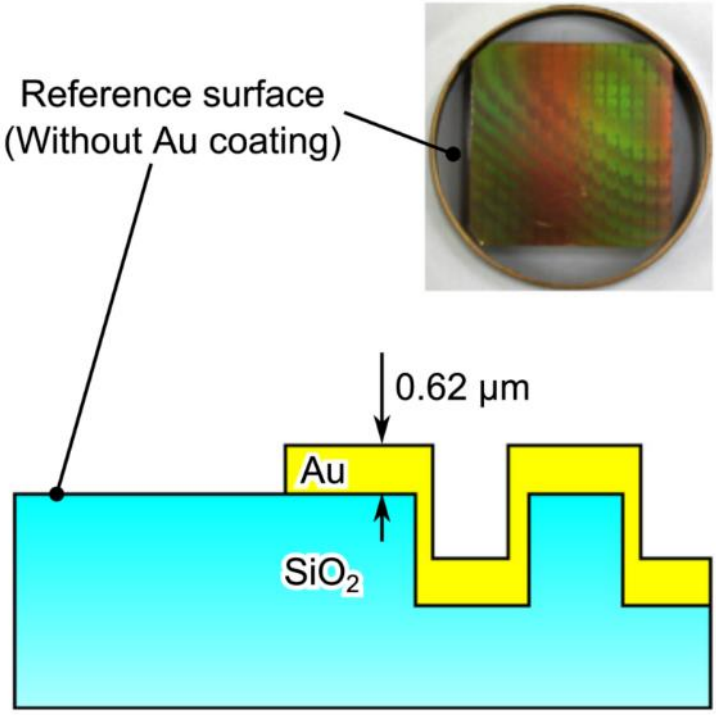

Figure 3.16: The gold-coated cavity emitter/receiver comprises a chamber with reflective gold-coated inner surfaces [12].

The receiver substrate was connected to a copper plate of 2 mm thickness, which had five holes for measuring the gap thickness using white light. It was thermally attached to the vacuum chamber wall which acts as a heat sink and maintains a low temperature. The experiment investigated the impact of rectangular microcavity arrays on radiative transfer between planar plates, comparing cases with and without a gold-sputtered coating, and found a significance increase in heat transfer when the separation distance was less than 3 μm.

In figure 3-17, the results demonstrated a difference in radiative flux between the emitter and receiver when microcavities were present, showing a notable effect on the gap-dependent heat transfer.

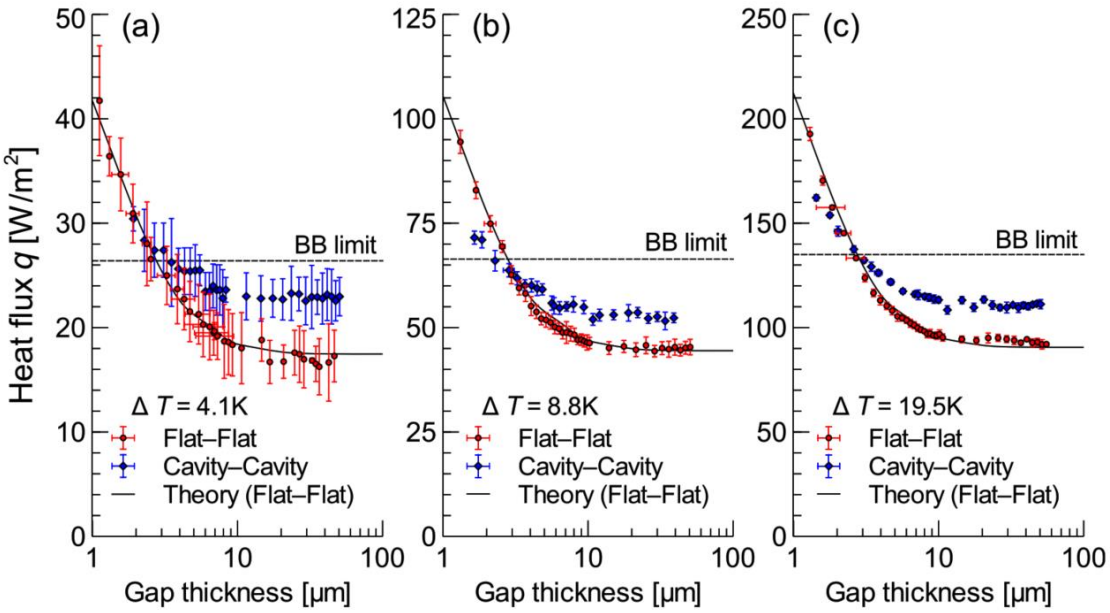

Figure 3.17: The measured radiative heat flux for different gaps. The solid black lines show theoretical predictions. The temperature gradients are (a) 4.4 K, (b) 8.8 K and (c) 19.5 K while the receiver plates temperature is at 303.7 K [12].

For large gap sizes, (i.e., in the far-field heat transfer regime), the heat flux was approximately 1.2 times greater than that for flat surfaces without microcavities. The near-field heat flux in the presence of the cavities was relatively low for small gaps. This suggests that the microcavities scatter thermal radiation and prevent total internal reflection, thereby reducing the near-field effect. However, these engineered microstructures convert a portion of the near-field energy into far-field energy, resulting in enhanced heat flow in the far-field region.

Bernardi *et al.* [55] conducted an experiment on radiative heat transfer for a temperature differences up to 120 K using a custom-made apparatus. The device consisted of two 5×5 mm^2 Si substrate separated by four, 3.5 μm tall SU-8 posts. After applying vertical force, the two substrates went into contact by SiO_2 stoppers which have a diameter of 5 µm and a vertical length of 150 nm to maintain a minimum gap distance. These stoppers prohibit further vertical movement of the substrates under applied force, as shown in figure 3-18.

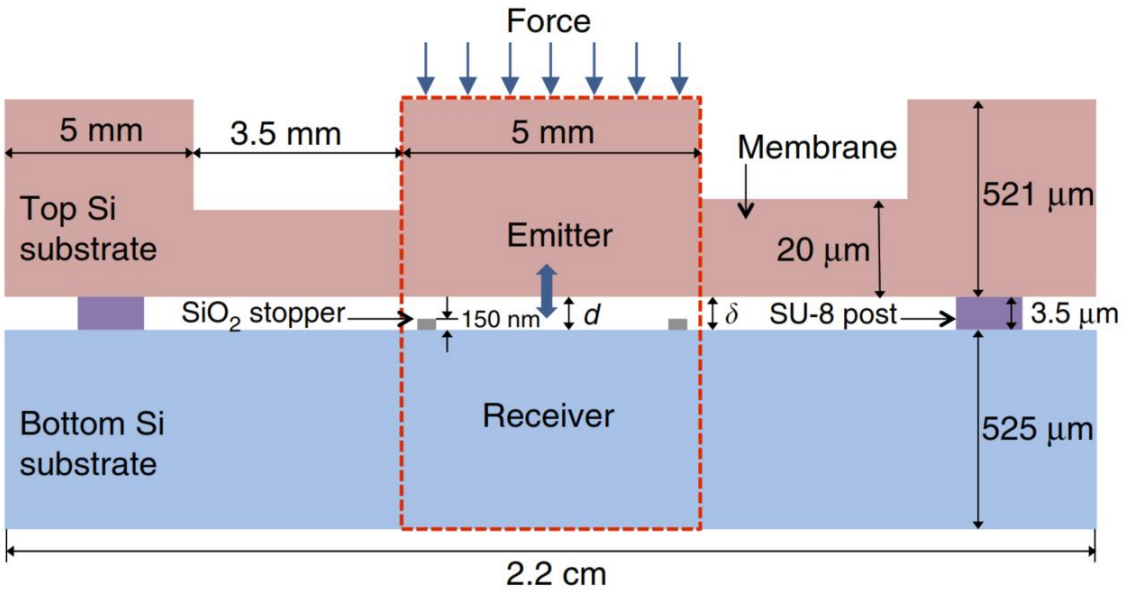

Figure 3.18: Two Si substrates are separated by 3.5 μm tall SU-8 posts. The SiO2 stoppers have a height of 150 nm [55].

The bottom substrate was made of a thin intrinsic Si wafer with a thickness of 525 μm. The top substrate was made from a Si-on-insulator wafer with a thickness of 521 μm. The surface of the Si substrates was smooth, with a roughness of less than 1.2 nm. To create a compliant structure, a trench measuring 501 μm in depth and 3.5 mm in width was etched on the lower-side of the top Si substrate using deep-reactive ion etching and a buffered oxide etch solution. This resulted in a

flexible Si membrane with a thickness of 20 μm, allowing a vertical movement between the 5×5 mm^2 emitter and receiver when an applied force is present. To maintain a temperature difference, thermoelectric (TE) modules were used. These modules acted as a heat pump on the hot plate side and a cooler on the receiver side. The TE heat pump was placed on a 500 µm-thick copper (Cu) heat spreader, which was located on the 5x5 mm^2 Si emitter. The temperature of the emitter was monitored using a thermistor embedded in the Cu plate. On the receiver side, the outer surface was kept at a temperature of 300 K and monitored by another thermistor. A 500 µm-thick Cu heat spreader separated the receiver and the TE cooler. The entire experimental setup was placed on a Cu heat sink, which was mounted to the base of the vacuum chamber. To ensure minimal contact resistance, thermal grease was used.

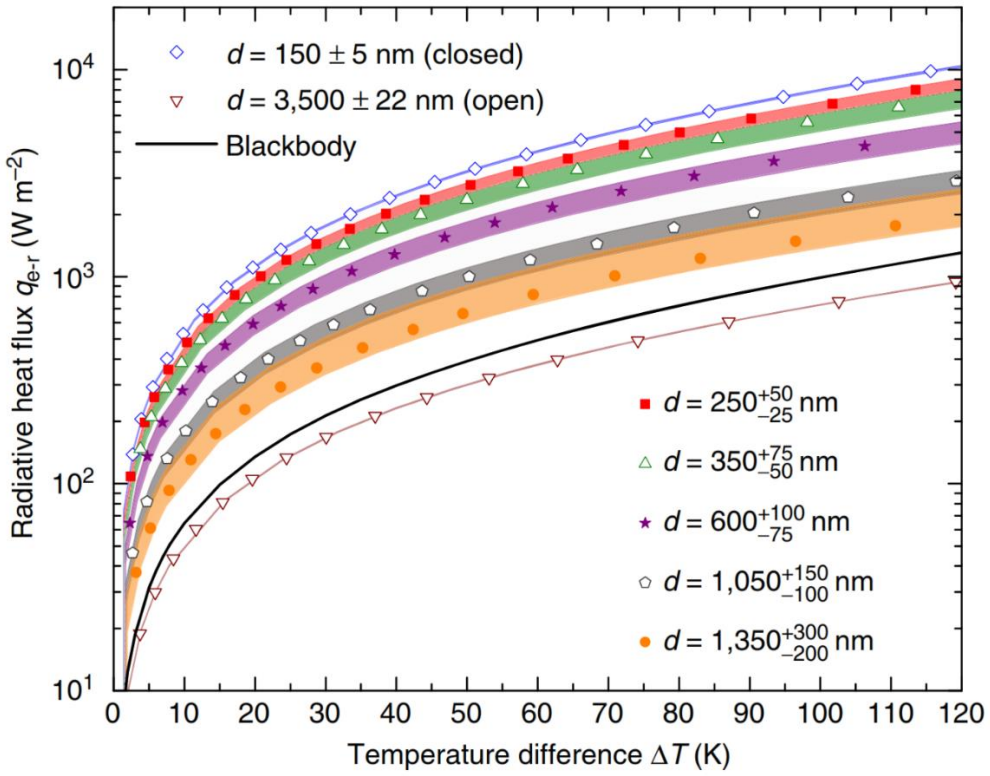

Figure 3.19: The radiative heat flux between two Si Substrates for different temperature gradients. The shaded region are theoretical predictions [55].

Figure 3-19 shows the experimental results of radiative heat flux surpassed the blackbody limit by a factor of 8.4 for 150 nm gap distance and a temperature gradient of 115.6 K. The far-field radiative heat flux measured at a gap distance of 3.5 μm is below the blackbody radiation limit. Watjen *et al.* [35] reported near field radiative heat transfer measurement between two 1×1 cm^2 doped-Si plated. The experimental gap distances varied from 200 nm to 780 nm and the temperature gradients were from 2 K to 30 K. A thermopile type heat flux meter was used to measure heat transfer. The experimental setup was surrounded with Aluminum foil as a radiation shield. The gap distance were established by depositing an array of SU-8 posts on of the surfaces as shown in figure 3-20. These nano pillars were fabricated on the SiO_2 using UV photolithography. A vacuum pressure of 3×10^{-4} Pa was established to ensure no convection heat transfer.

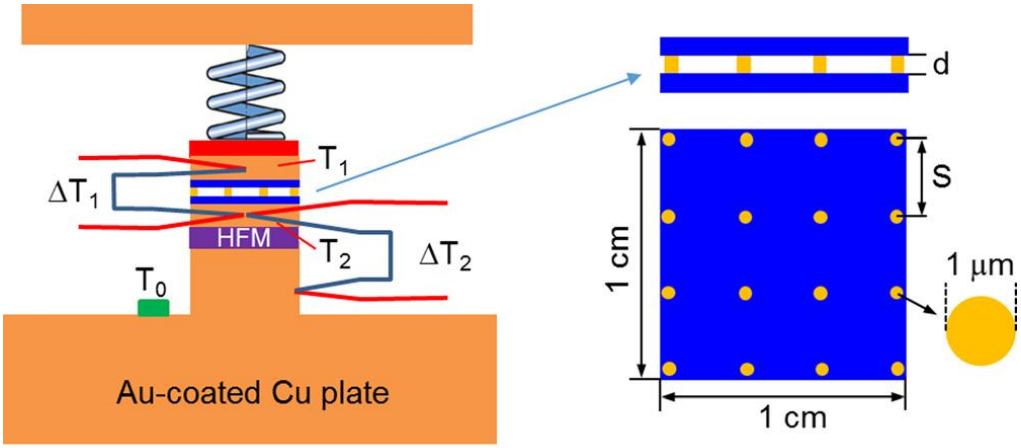

Figure 3.20: (a) Schematics of the experimental setup used in Ref. [35]. (b) A schematic of the array of SU-8 posts fabricated on the doped Si plates [35].

There was uncertainty about the vacuum gap size due to residual bow or warp and non-uniformity of the post's heights. In calculations, they considered gap sizes of 30 – 90 nm to account for this

uncertainty. Figure 3-21 shows the measured heat flux [14]. It is seen from Fig. 3.21 that radiative heat transfer decreases with increasing the gap distance. They used up to 200 mN force to control the gap distances on the substrates and reported a 11 times radiative heat transfer enhancement over the blackbody radiation limit at a gap of 200 nm.

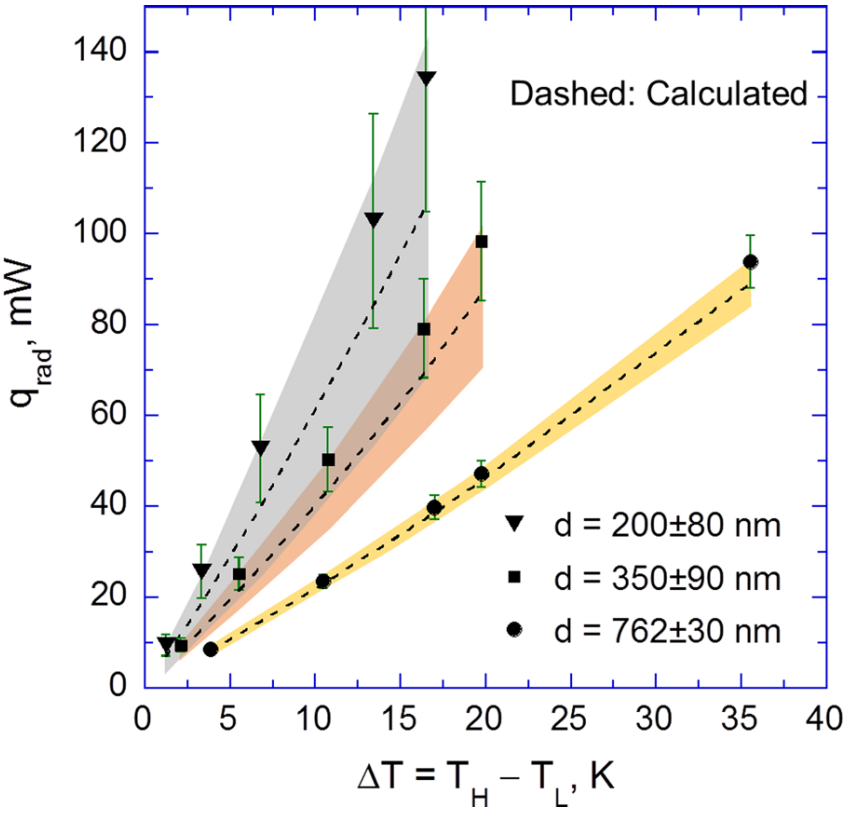

Figure 3.21: Radiative heat transfer between two doped Si plates versus the temperature gradient for three different gap distances. The shaded regions are the uncertainty associated with the lack of knowledge of the exact value of the gap distance [35].

DeSutter *et al* [34] used micropillars to experimentally measure NFRHT between doped-Si surfaces. They manufactured an NFRHT device using lithography. The emitter plate and the receiver plate were manufactured from boron doped Si which are separated using SU-8 pillars. Figure 3-22 shows the micropillars that are deposited within pits etched into the emitter, forming

a 2×2 or 3×3 array with a diameter of ~ 20 μm or 30 μm. Both the receiver and the emitter have 5.2 × 5.5 mm^2 surface area and a thickness of 525 μm. A protective frame is etched into both the emitter and receiver substrates to safeguard against particle contamination, ensuring the desired gap spacing. The height of the micropillars and the depth of the pits determine the actual gap between the emitter and receiver. They determined the gap distance using SEM. The experiment was conducted inside a vacuum chamber with a 5×10^{-4} Pa vacuum pressure.

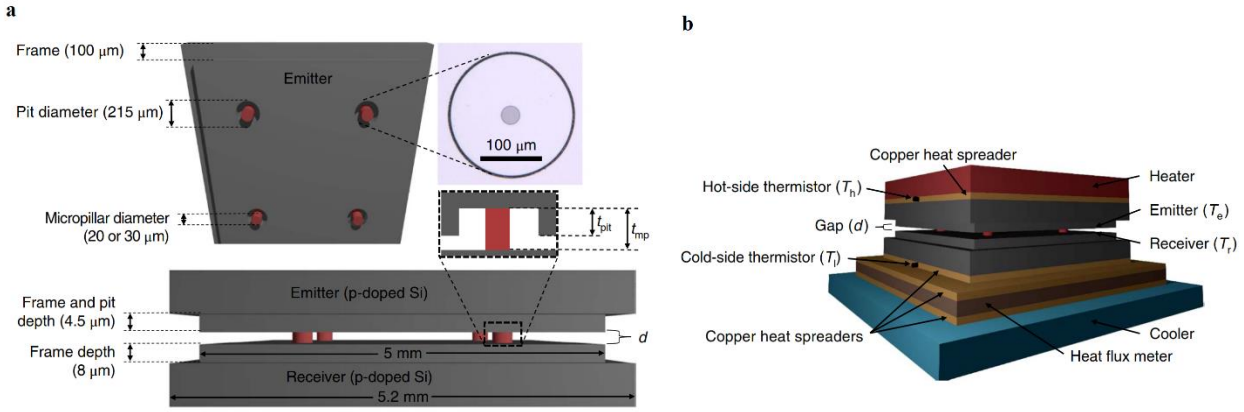

Figure 3.22: (a) The NFRHT device comprised of a doped Si emitter and receiver, separated by a vacuum gap formed by depositing SU-8 micropillars on the emitter. (b) The heat transfer measurement setup consists of a thermoelectric heater, thermistors embedded in copper plates, a heat flux meter, and a thermoelectric cooler [34].

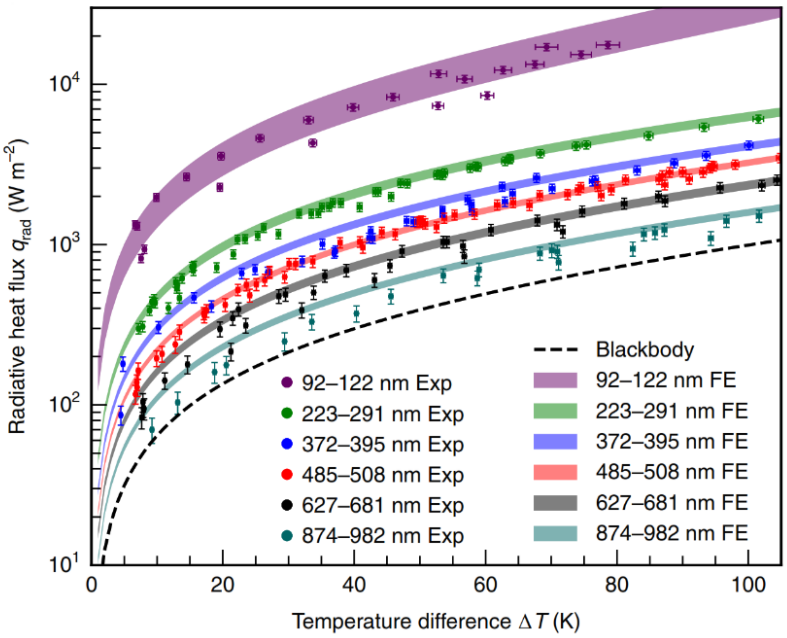

Figure 3.23: The experimental results for radiative heat flux versus the temperature difference, ΔT, for six different gap distances varying from approximately 90 nm to 1,000 nm. The color shaded area represents the theoretical predictions calculated using fluctuational electrodynamics (FE). The error bars associated with the experimental data account for uncertainties in the measured heat rate and temperatures. [34].

The rate of heat flow across the device is a combination of conduction through the micropillars and radiation between the emitter and receiver. For the largest gap with a size of 874 – 982 nm, the estimated contribution of conduction to the overall heat transfer is approximately 22–35%. In contrast, for the smallest gap with a size of 92 – 122 nm, the contribution of conduction reaches a minimum of around 1.9 – 4.1%. Figure 3-19 shows that the narrowest vacuum gap spacing (92-122 nm) exhibits a remarkable radiative heat transfer amplification of approximately 28.5 times

compared to the maximum blackbody radiation due to thermal emission of SPPs from the doped Si plates.

Ying *et al.* [56] conducted experimental measurement of radiative heat transfer in the near-field regime between doped silicon chips measuring 1×1 cm^2, separated by vacuum gap distances of 190 ± 20 nm, 345 ± 29 nm and 507 ± 47 nm achieved by SU-8 nano pillars for various temperature differences of 25 K to 85 K. The doping level of Si plates were maintained at 2×10^{19} cm^{-3}. To minimize conduction effects, they employed SU-8 polymer posts with varying heights (Figure 3-24a), reducing conduction to less than 6% of the total heat transfer as a result of the polymer's negligible thermal conductivity. The estimation of vacuum gaps ranging from 507 ± 47 nm down to 190 ± 20 nm were done by using capacitance measurement inside a vacuum environment of 0.1 Pa.

In Figure 3-24b, the experimental setup for near-field measurements is schematically shown. Three thermistors with a resolution of 0.1 °C are employed to measure the temperature of the emitter (T_1), the top surface temperature of the receiver glass slide (T_2), and the bottom surface of the glass slide (T_3). The emitter sample was separated from the receiver using SU-8 posts (Figure 3-24a). To maintain pressure on the emitter, a copper plate was used as a heat spreader and a ceramic heater with a total weight of 3.23 g were placed on top, resulting in a pressure of 316.8 Pa. Thin bonding wires were attached to the receiver plate surface and the top copper plate using silver paste. The top copper plate was connected to the emitter plate electrically through carbon tape for measuring capacitance of the gap using a multimeter. From an optical image, the estimated overlapping region between the emitter and receiver samples accounts for approximately 70% of the total sample size.

They fabricated 52 SU-8 posts with a diameter of 3 μm on the receiver Si substrate. Before fabricating the SU-8 posts, they cleaned the surface by O_2 plasma etching and used photomask on a spin coated Si substrate to obtain nano pillars. After that, it was exposed to UV light followed by a hard baking at 150 ℃.

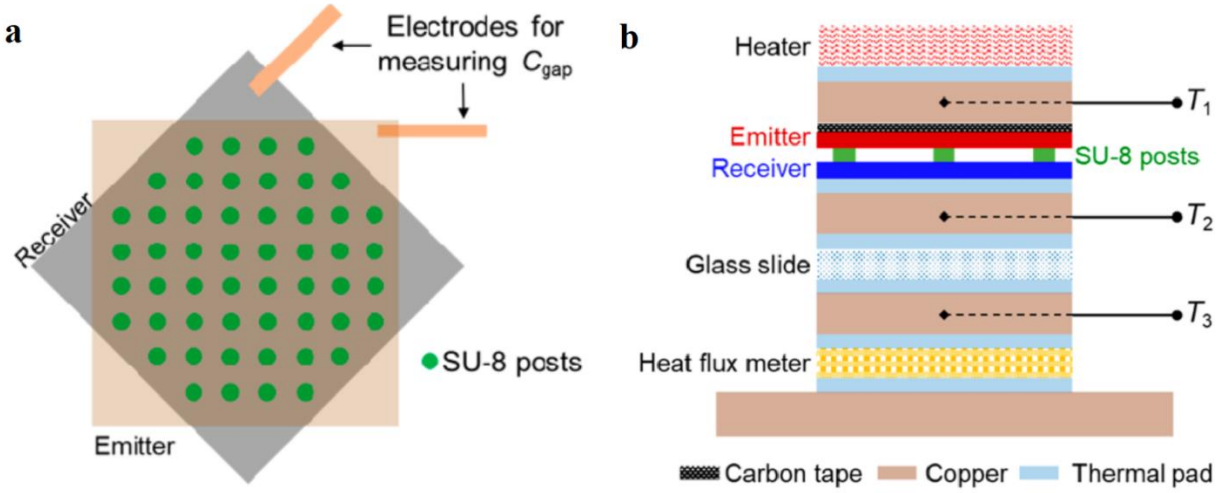

Figure 3.24: (a) Schematic of SU-8 nano pillars. (b) NFRHT experiment setup [56].

Figure 3.25 shows the experimental data. An 11-fold enhancement in radiation heat transfer at a gap distance of 190 nm compared to the maximum blackbody radiation is measured.

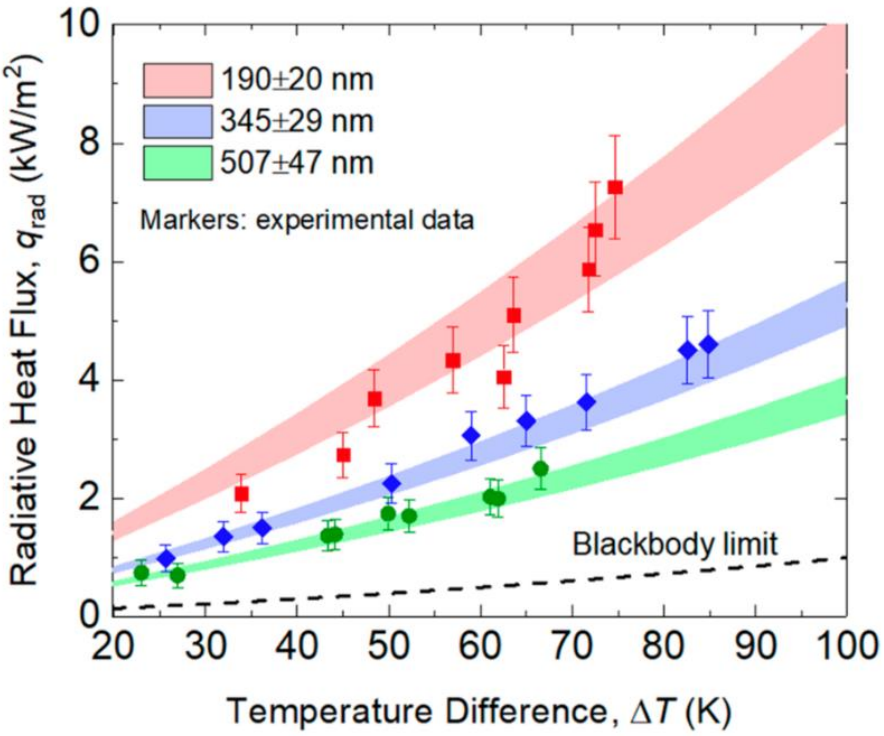

Figure 3.25: The experimental and theoretical near-field radiative heat flux for three different vacuum gap distances is plotted against the temperature difference of the emitter and receiver. The blackbody limit is also included for comparison [56].

The theoretical modeling of NFRHT using fluctuational electrodynamics suggests that enhanced radiative heat transfer is due to thermal emission of SPPs in the *p*-polarization.

CHAPTER 4

EXPERIMENTAL SETUP FOR MEASURING RADIATIVE HEAT TRANSFER BETWEEN TWO PLANAR MEDIA

4.1 Device Setup

Figure 4.1 shows the experimental setup implemented for measuring the radiative heat transfer between two planar media. The two plates are separated by a spacing material. A copper plate with a thermocouple inserted inside is attached to the top of the emitting medium (emitter) which is heated by a Thorlabs 20 mm × 20 mm ceramic heater. A heat flux meter is attached to the bottom surface of the receiving medium (receiver) to measure heat transfer. A second copper plate is placed beneath the heat flux meter to distribute heat evenly. A T-type thermocouple is embedded in the copper plate to measure the temperature of the receiver. A TEC is attached to the bottom copper plate to remove heat from the system. TEC removes heat from the system to an aluminum heat sink to keep the receiver at a constant temperature.

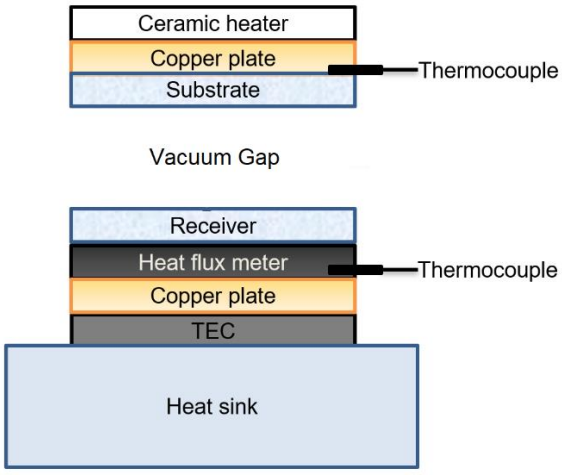

Figure 4.1: A schematic of the setup implemented for measuring the radiative heat flux between two planar media .

Figure 4.2 shows a U-block which is used to keep the materials in place. As it can be seen from Fig. 4.3a, a spring is used with the U block and a cork is placed between the spring and the heater to omit heat transfer loss in Figure 4.3a.

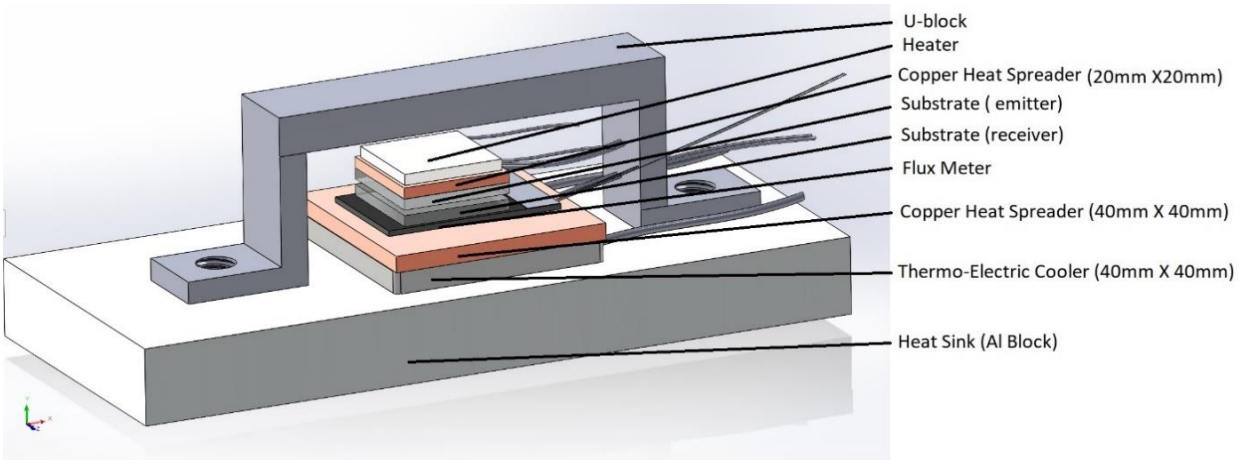

Figure 4.2: A 3D schematic of the experimental setup.

COMPAQ DAQ data acquisition system is used for readings from a heat flux meter (fluxteq PHSF – 01e) which measures the heat flux for a given temperature difference. The heat flux meter has an embedded thermocouple. A custom-made vacuum chamber (Kurt J. Lesker) is used to maintain vacuum pressure for the experiments. All electric and sensor cables pass through a vacuum feed through (Figure 4.3b).

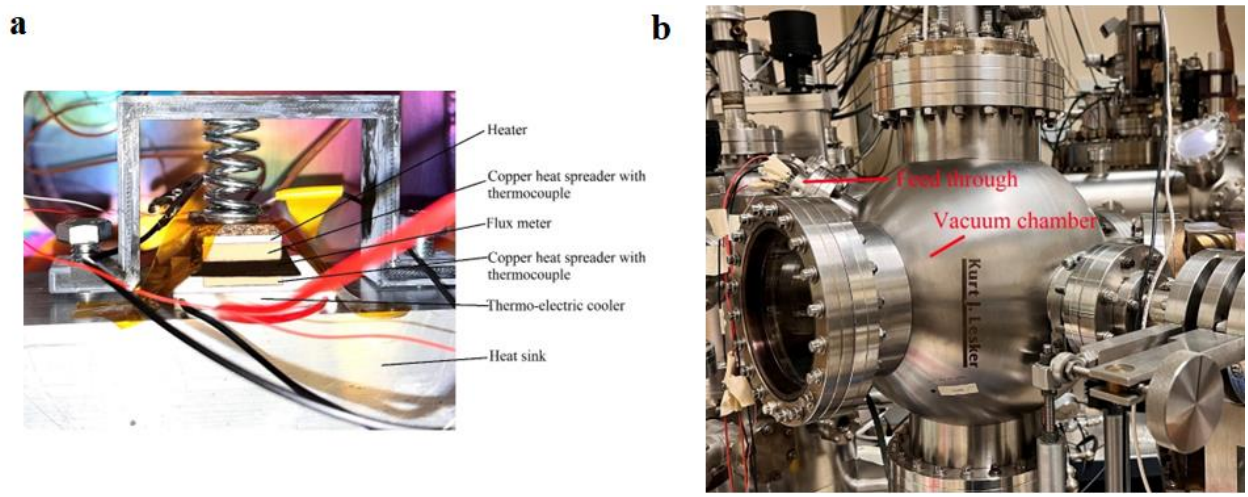

Figure 4.3: (a) A photograph of the Experimental setup. (b) The vacuum chamber used for the experiments.

4.2 Temperature Close-loop Control

The control system is an automated self-regulating system that uses a thermoelectric device, the heater, and the thermocouple to maintain a desired temperature gradient. Arduino is used for the automatic control of the temperature gradient. It comprises of two thermocouples, thermocouple amplifiers, D/AC, resistor, MOSFET, heater, TEC, and power supply.

Figure 4.4 shows that the sensor takes reading of the temperature and feeds it to Arduino microcontroller. Then, the microcontroller compares the reading from the sensor with the setpoint and then adjusts the voltage and current to control heater and TEC. The temperature sensor can take readings of the temperature from 0 ℃ to 105 ℃.

The close loop control consists of several electric components. Table 2 shows the name of the components and specifications.

Table 4-1: The electrical components used for constructing the control system and their specification.

Name of Components	Description
Power supply	12 VDC output
Resistors	10 KΩ
Arduino	Arduino Mega 2560
Digital to analog converter	DAC0808
MOSFET	IRL3103
Thermocouple amplifier	MAX31856
Heater	HT24S
Thermoelectric cooler	TEC1-12706

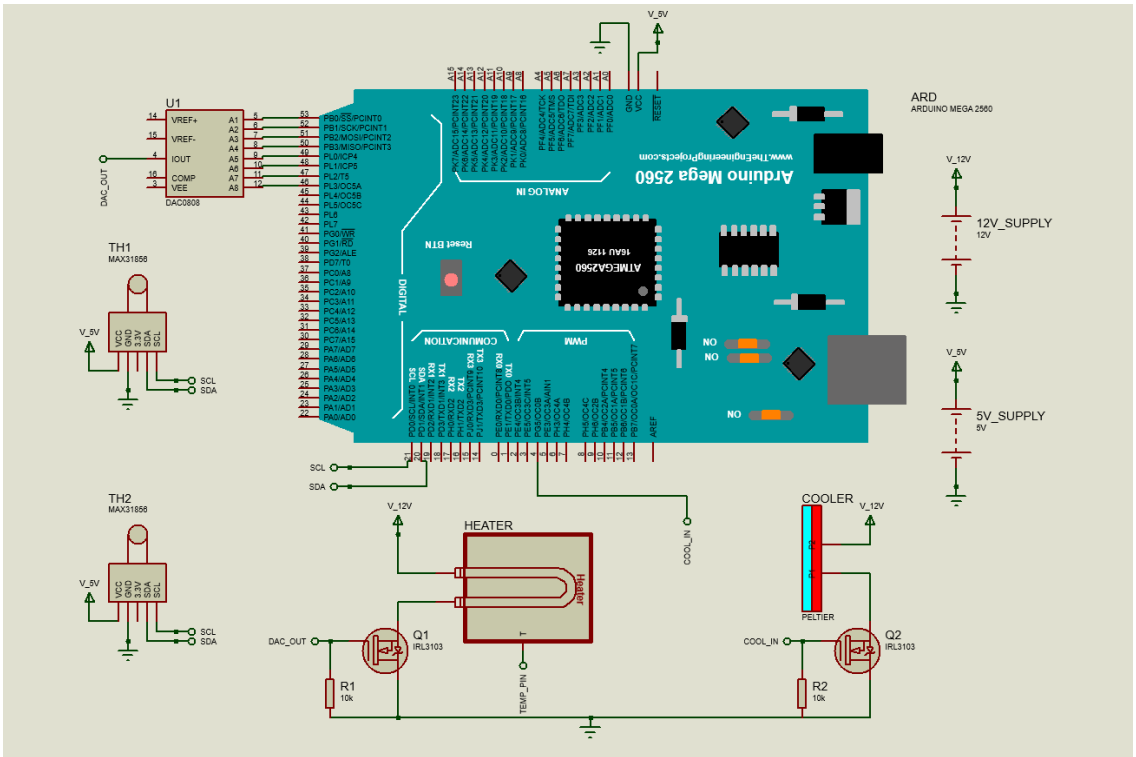

Figure 4.4: Schematic diagram of the temperature control system simulated using proteus.

The most fundamental component used for signal processing and transmission is the Arduino 2560 Mega microcontroller, which is based on ATmega2560. It has 54 digital input/output pins and 16 analog inputs. It has built-in serial communication interfaces and USB cable that can be used for connection with PC. Through the USB cable attached to the computer, the code is compiled in the Arduino IDE and uploaded to the Arduino board. The code allows us to set the temperature of the heater and the TEC. Then Arduino adjusts voltage and current supply to maintain the set temperatures.

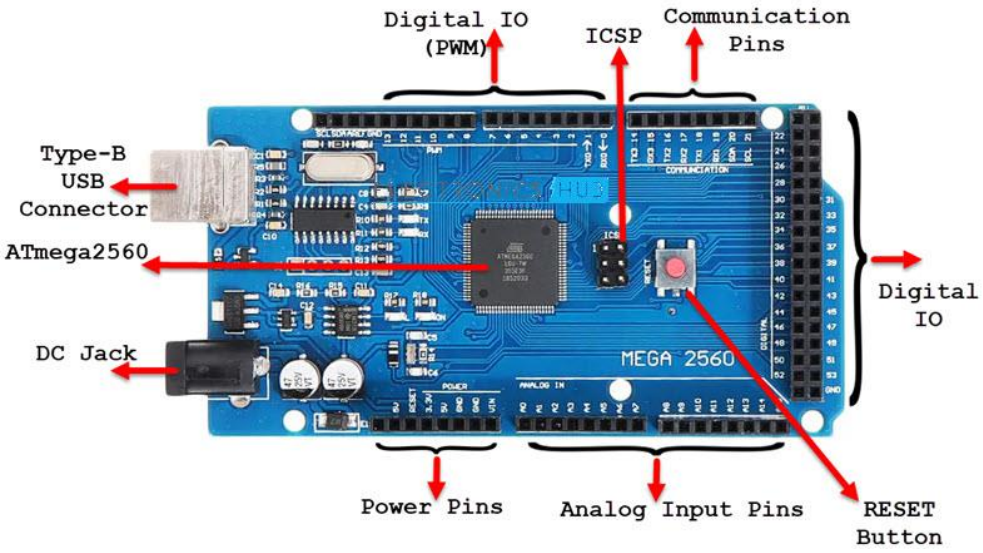

Figure 4.5: Arduino Mega 2560 Microcontroller Board [57].

The T-type thermocouple and universal thermocouple amplifier (MAX31856) manufactured by Adafruit are used with Arduino Mega for measuring temperature.

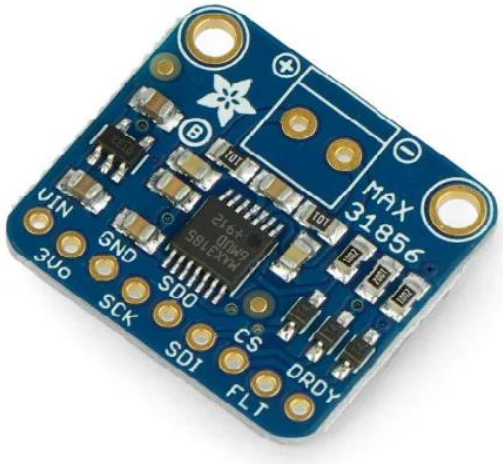

Figure 4.6: Thermocouple amplifier MAX31856 [58].

Thermocouples are very sensitive and require a reliable amplifier. The MAX31856 board comes equipped with its own chip, a 3.3V regulator and level shifting circuitry. It offers an easy interface with any microcontroller model and supports T-type thermocouple. The board has internal temperature reading capabilities and can provide temperature output ranging from $-210℃$ to $+1800℃$. In figure 4.6, the SCK pin is used as the input for the SPI clock, SDO is responsible for data transmission from the processor to MAX31856, and CS acts as the chip select pin. The FLT and DRDY pins on the board have additional functionalities for advanced use. Four Arduino digital I/O pins connect with the logic pins of the board.

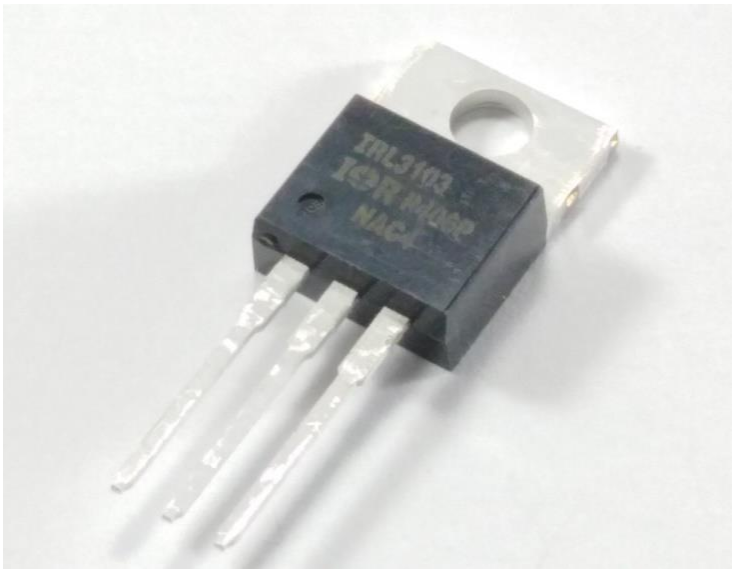

Figure 4.7: N – channel MOSFET transistor.

To control heating and cooling, we used a ceramic heater and a thermoelectric cooler, power supply, resistor (10 KΩ) and N-channel power MOSFET transistor as shown in the figure 4.7. The Heater consumes 24 W at 12V, 6.1W at 12V and 1.5W at 6V. The heater is chosen because of its low power consumption, and it can be heated up to 400℃. The heater and the TEC are supplied with external power supply as Arduino cannot provide high voltage. The TEC can maintain up to 75℃ temperature gradient. In addition, the N-channel power MOSFET transistor can switch over 64A and 30V for pulse width modulation heat control.

CHAPTER 5

RADIATIVE HEAT TRANSFER BETWEEN TWO BLACKBODIES

The objective of this chapter is to calibrate and utilize a flux meter in a radiative heat transfer experiment. This will be achieved by employing black paint, known for its emissivity close to 0.95, to coat two copper plates. The black-painted Cu plates will act as blackbodies. These plates will be positioned in parallel with a 1 mm vacuum gap between them. The primary goal is to measure the radiative heat transfer within a vacuum environment and compare the experimental emissivity of the black paint with its known emissivity.

A blackbody is an idealized object that absorbs all incident radiation across all wavelengths without reflecting or transmitting any of it. The radiative heat transfer between two planar media separated by a gap greater than the thermal wavelength (i.e., a far-field gap) is found using the *Stephan-Boltzmann* law as [59]:

$$Q = \varepsilon\sigma A(T_1^4 - T_2^4) \tag{5-1}$$

Where ε is the emissivity of the surface, $\sigma = 5.67 \times 10^{-8} \frac{W}{m^2 K^4}$ is the *Stephan-Boltzmann* constant, T_1 and T_2 are the temperatures of the two media, and A is the surface area. We used *Stephan-Boltzmann* law to validate our experimental setup in vacuum condition. Heat transfer measurement between two blackbodies is conducted using setup showing in Figure 5.1 located inside a vacuum chamber at a 6.4×10^{-6} Torr pressure.

Both plates have a surface are of 2020×20 mm^2 and a thickness of 2 mm, and the plates surfaces are covered with blackbody paint (VHT-SP102). The emitter (top plate) is heated by a heater and a TEC was attached to the bottom surface of the receiver plate (bottom plate). Two thermocouples were inserted in the middle of the copper heat spreader to measure the emitter and receiver plate temperature. One copper heat spreader was on top of the emitter plate and the other one was

between the receiver and TEC. These two blackbodies were separated by two small cork pieces which have approximately a total surface area of 0.000012 m^2, a thickness of 1 mm and a thermal conductivity of 0.03 W/mK.

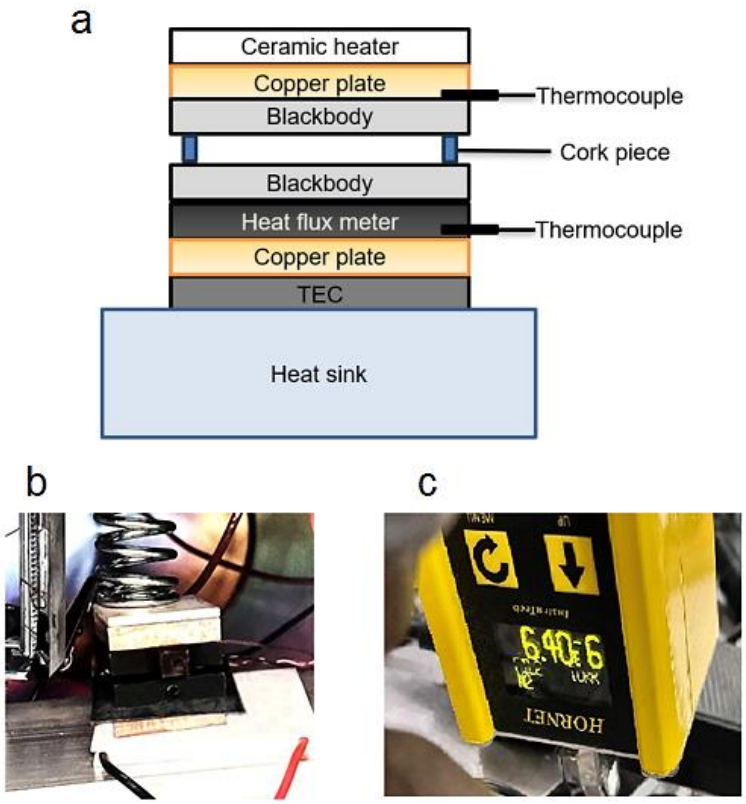

Figure 5.1: (a) Schematic of experimental setup used for measuring the radiative heat flux for two blackbodies. (b) Two Cu plates sprayed with blackbody paint separated by a 1 mm gap distance established using cork material. (c) Vacuum pressure (6.4×10^{-6} Torr) of the chamber.

Heat conduction through cork is calculated using steady-state heat transfer assumption:

$$Q = \frac{k}{t} A \Delta T \quad (5\text{-}2)$$

Where, Q is conductive heat transfer in watts, k the is thermal conductivity of the material, t the is material thickness and A is the heat transfer area. The total heat flux is the sum of heat transfer due to thermal radiation between the blackbodies and heat conduction through the corks.

Table 5-1: Theoretical calculation of the total heat flux due to thermal radiation and conduction through the cork pieces for different values of emissivity of the black paint and thermal conductivity of cork.

ε – Emissivity of the black paint	**K – Thermal conductivity of Cork** [60] **(W/m.K)**	**q – Total heat flux (Wm^{-2})**
0.9	0.03	206
0.95	0.03	216
0.94	0.04	225
1.0	0.04	235

The emitter plate temperature is 50℃ and the receiver plate temperature is 20℃. The total heat transfer from the emitter blackbody to the receiver blackbody is contributed by both radiative heat transfer between them and conduction through the cork portion. Table 5-1 shows that the total heat transfer is between 206 Wm^{-2} to 235 Wm^{-2} depending on the emissivity of the paint and thermal conductivity of cork. To maintain vacuum gap distance, two cork pieces were used and each piece has a rectangular cross section with an area of 6 mm^2 which results in a total area of 0.000012 m^2. A conduction contribution of $\sim$15% is estimated for this 0.000012 m^2 surface area.

Table 5-1 illustrates that the experimental heat transfer is 219 ± 5 Wm^{-2}. Comparing this experimental data and the theoretical calculations, it can be concluded that emissivity of the blackbody paint is between 0.93 – 0.95. Since the theoretical and experimental results are in good agreement, it can be concluded that the implemented setup can be used for accurate measurement of the radiative heat flux between two planar media.

CHAPTER 6

NEAR-FIELD RADIATIVE HEAT TRANSFER EXCEEDING THE BLACKBODY LIMIT

Near-field radiative heat transfer between two planar media will be experimentally measured in this chapter, and it is shown that the NFRHT can exceed the far-field blackbody radiative heat transfer limit substantially.

6.1 Near-Field Radiative Heat Transfer Between Two Quartz Plates Separated by Polystyrene Particles

6.1.1 Introduction

In this chapter, we experiment with the near-field radiative heat transfer between two macroscale flat surfaces using polystyrene particles to maintain gap distance. The use of polystyrene particles enables establishing a nanoscale gap between the two surfaces while contributing negligible heat conduction to the total heat transfer. These nano-sized polystyrene particles are placed between the two flat plates. The gap distance between the two surfaces will be equal to the diameter of the polystyrene particle. By optimizing the distribution of the particles on the surface, we can control the gap distance between the surfaces. Since the particles are transparent, it is expected that they do not interact with the thermal radiation emitted by the surfaces, and thus do not modify the local electromagnetic field distribution. The nano-sized particles are used in this study as this approach for establishing a nanoscale gap between two planar media is relatively simple.

6.1.2 Experimental Procedure

The vacuum gap distance between quartz plates in this experiment is maintained using polystyrene particles as illustrated in Figure 6.1. The polystyrene particles are adopted since they have a low thermal conductivity. Additionally, polystyrene particles are transparent in the infrared region of

the electromagnetic spectrum, and thus they do not interact with thermal radiation from the planar media. We use polystyrene spheres with dimeters of 100 nm and 200 nm to establish two gap distances.

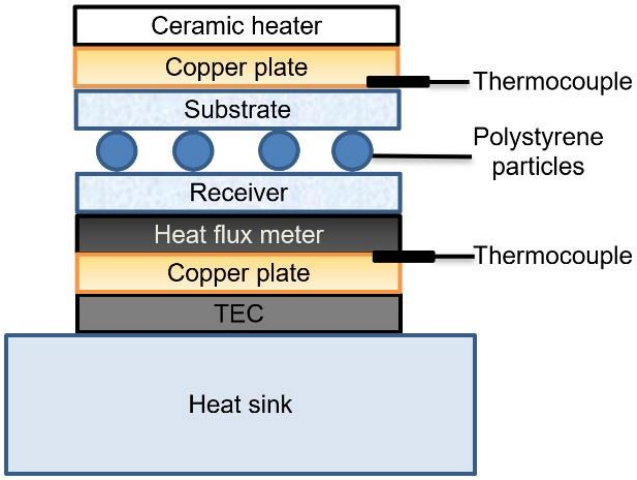

Figure 6.1: Diagram illustrating the experimental configuration. A nanoscale gap is maintained between the two media by depositing polystyrene nanopartciles on one of the media.

Figure 6.2 shows SEM images of the polystyrene particles of diameters 100 nm and 200 nm provided by the vendors [61]. The polystyrene nanoparticles have a deviation of ~5 nm in diameter. To create a uniform suspension and prevent aggregation, a two-step dilution process was carried out using a sonic bath sonicator and magnetic stirrer.

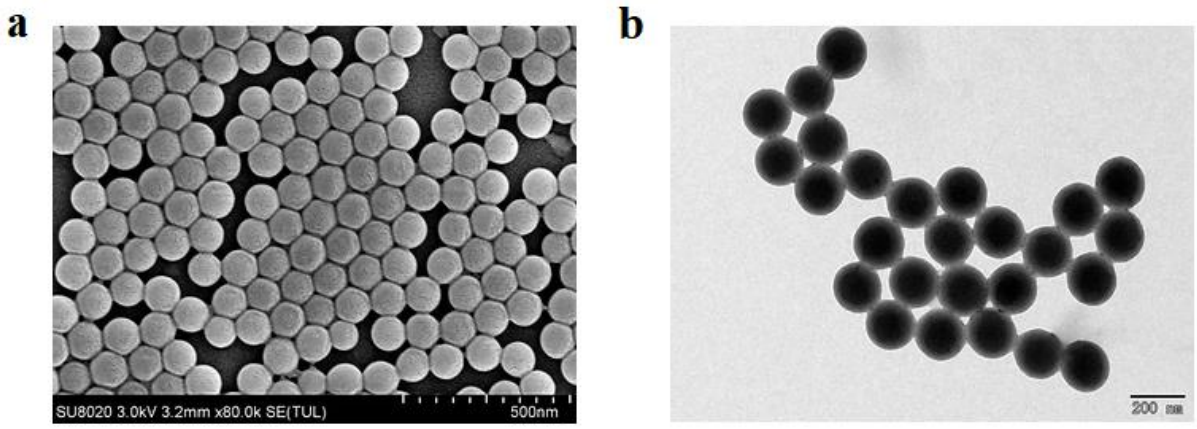

Figure 6.2: Scanning electron micrographs of (a) 100 nm polystyrene particles. (b) 200 nm polystyrene particles [61]. The pictures are taken from the vendor's website.

We purchased polystyrene particles solution from Alphananotechne with a concentration of 10 ml at 10 mg/ml. First, we take a drop (0.06 ml) of the purchased solution using a syringe and mix it with 50 ml of DI water. Then, a drop (0.06 ml) of diluted suspension was mixed with 100 ml of DI water again for further dilution. By performing the dilution process two times, the particle concentration was reduced to 6-7.8× 10^6particles/mL, which allowed for the desired vacuum gap to be created while minimizing conduction heat transfer. Approximately 80 thousand polystyrene nanoparticles from the diluted solution were deposited onto the surface of the receiver sample using a syringe. If uniform deposition of particles on the surface is assumed, the distance between the particles is 22 μm. The total surface area of the deposited particles is less than 0.5% of the surface area of the substrate. The substrate was then heated on a hotplate to evaporate the water. After that, the substrate was inspected for large particle aggregation and dust particles. Figure 6.3 shows an optical microscope image of the surface of the receiver substrate. It is seen that the surface is cleaned, and the impurities are inside the substrate.

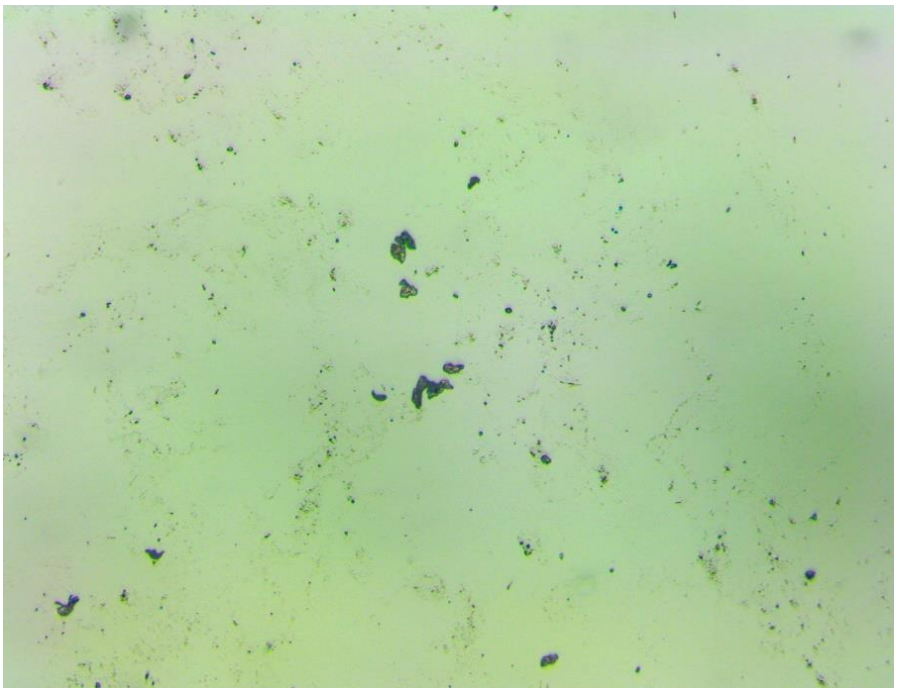

Figure 6.3: Optical image of deposited nanoparticles over a quartz substrate.

The temperature of the emitter and receiver plates were recorded using T-type thermocouples. The data from the heat flux meter was taken after the heat transfer reached steady-state condition. Thermal paste was used between plates to achieve uniform heat distribution.

6.1.3 Results and discussion

The measured heat flux versus the temperature difference is shown in Fig. 6.4. The measured data clearly shows that the experimental heat flux exceeds the blackbody radiation limit. The temperature differences were from 15 K to 90 K between the emitter and the receiver substrate, while the emitter surface temperature is kept at 293 K under the vacuum condition of $6 - 7 \times 10^{-6}$ Torr for both 100 nm and 200 nm gap distance. We used Turbo-V 301 vacuum for achieving the vacuum pressure inside the chamber. For 100 nm gap distance, Figure 6.4 shows that the measured radiative heat flux is 9-fold greater than the blackbody (maximum) radiation and for the 200 nm gap distance, the results were 3 times more than the blackbody radiation. The enhancement of the

heat transfer is due to the contribution of evanescent modes, particularly the surface phonon polaritons supported by the quartz plates, to the radiative heat transfer in the near-field regime.

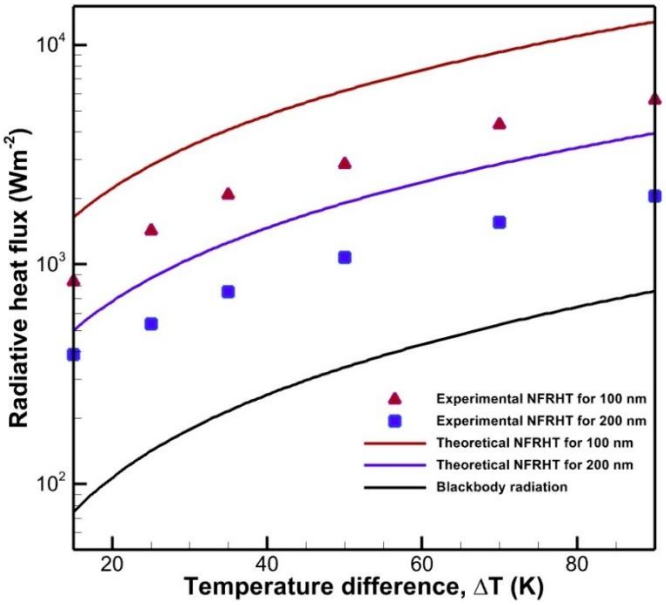

Figure 6.4: Temperature dependent radiative heat transfer.

The non-negligible difference between the measured and theoretical heat flux in our study is caused by several factors. Firstly, we encountered difficulties in achieving the desired gap distance due to the coagulation of the polystyrene particles in some areas of the surface. The formation of these particle clusters prevented the formation of a uniform monolayer of particles, which is crucial for achieving an exact gap distance equal to the diameter of the particles. Furthermore, the variation in surface roughness of the substrates contributed to the deviation of the experimental results from the theoretical predictions. The presence of surface irregularities affected the total gap distance between the two flat plates, leading to inconsistencies in heat transfer measurements. To address these difficulties and achieve a more uniform and controlled gap distance, we decided to employ an alternative approach utilizing nanofabrication techniques. By etching nano pillars on the substrate using nanofabrication methods, we can precisely control the height and number of these pillars, thus ensuring a desired and consistent gap distance between the emitter and receiver

substrates. This alternative approach and its implementation will be discussed in detail in the subsequent chapter.

6.2 Near-Field Radiative Heat Transfer Between Two SiC Plates Separated by SU-8 Nano-pillars

6.2.1 Introduction

In this section, we experimentally demonstrate NFRHT between two SiC plates separated by a nanoscale gap achieved by SU-8 nano pillars. Achieving a uniform vacuum gap between two parallel flat substrates for NFRHT is a challenging task. Using the photo-lithography technique, we fabricate nano pillars on one of the substrates in a uniform manner. In addition, the small surface area and low conductivity of the SU-8 posts results in negligible heat conduction between two substrates compared to the radiative heat flux. Using SU-8 nano pillars enables us to create nano-sized gaps between the two substrates and experimentally measure heat flux between them in the presence of a temperature difference.

6.2.2 Experimental Procedure

We fabricated a total number of 361 SU-8 nano pillars on a SiC substrate with a total surface area of $3 \times 3\ \mu m^2$. The thermal conductivity of the SU-8 is around 0.2 W/m.K [62]. Figure 6.5 shows the experimental setup developed to measure radiative heat flux in the near-field and far-field regimes. For the near-field measurements, the emitter and the receiver are separated by SU-8 nano pillars. The average height of the nano pillars is 175 nm. A thermoelectric cooler (TEC) is used to maintain a steady temperature for the receiver. A temperature of 293 K are selected for the receiver plate.

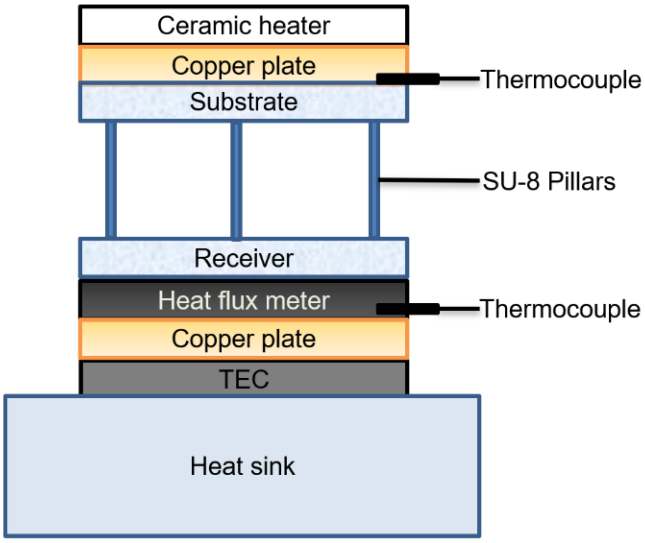

Figure 6.5: Schematic of the experimental setup. Thermocouples were inserted inside the Cu plates to take the temperature readings.

In the experimental setup, we use copper plates which are 2 mm thick and have a conduction thermal resistance of 0.325 K/W. Cu plates are utilized to evenly distribute the heat over the receiver plate. The temperature readings of the emitter and the receiver are measured by thermocouple inserted into the Cu plates. Thermal grease (Arctic Silver Ceramique 2) is used at all interfaces to minimize contact resistance. The setup was inserted inside a vacuum chamber. The vacuum pressure is maintained at approximately $1 - 9 \times 10^{-6}$ Torr for several measurement trials. The substrate size is selected to be 15 mm × 15 mm to fit into the measurement setup.

Under the steady-state conditions and by neglecting convective thermal loss, which is a reasonable assumption for the vacuum pressure in the experiments, the energy balance is $Q_{total} = Q_{rad} + Q_{cond,posts}$, where $Q_{cond,posts}$ is the heat conduction via SU-8 posts, Q_{rad} is the total radiative heat transfer and Q_{total} is the total heat transfer due to Q_{rad} and $Q_{cond,posts}$. The heat flux

experiments between the two parallel plates were measured by a heat flux sensor. The temperature of the heater and thermoelectric cooler (TEC) were controlled by an Arduino close loop control.

6.2.3 Heat Flux Measurement

The experimentally measured heat flux versus temperature gradient is shown in Figure 6.6. The experimental data shows that the results exceeded the blackbody radiation limit. The temperature differences were from 15 K to 70 K between the emitter and the receiver substrate while the receiver plate temperature was at 288 K and 293 K under the vacuum condition for 175 nm gap distance. We took the heat flux reading when the system reached the steady state condition. We consider approximately 15% of the total heat transfer as the heat conduction through the SU-8 posts. We repeat the heat transfer experiment on different days in order to make sure that our results can be reproduced.

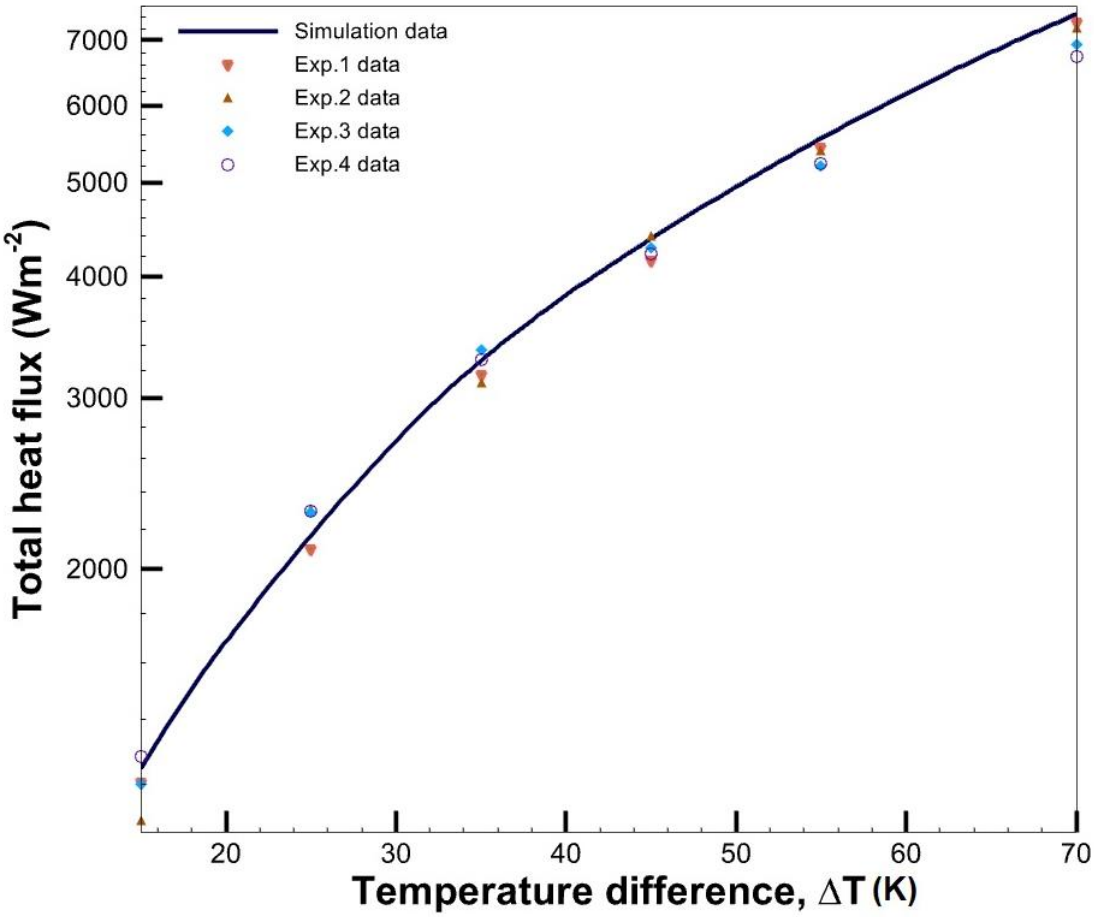

Figure 6.6: The heat flux between two SiC plates separated by a gap of 175 nm. The symbols show the experimental radiative heat flux (Exp.) for several experimental trials.

6.2.4 SU-8 Fabrications and Cleanliness

The main steps for fabricating the SU-8 posts on a SiC substrate are illustrated in Figure 6.7a. The fabrication process is done inside 1000 class cleanroom environments. Before depositing the SU-8 posts, the surface of the substrate is thoroughly cleaned with acetone in a sonicated bath for 5 minutes, followed by spraying with isopropanol for 1 minute, and finally washed with DI water to remove any debris. Then, it is dried inside an oven at 110℃ for 30 minutes. Next, the SiC is coated with photoresist and is spun at 3500 rpm for 30 seconds using a spin coater. The spin coating is

followed by a soft bake at 90℃ for 2 minutes. A photomask is used to expose the photoresist to ultraviolet light at 65 mJ/cm^2, which creates a pattern of SU-8 posts on the substrate.

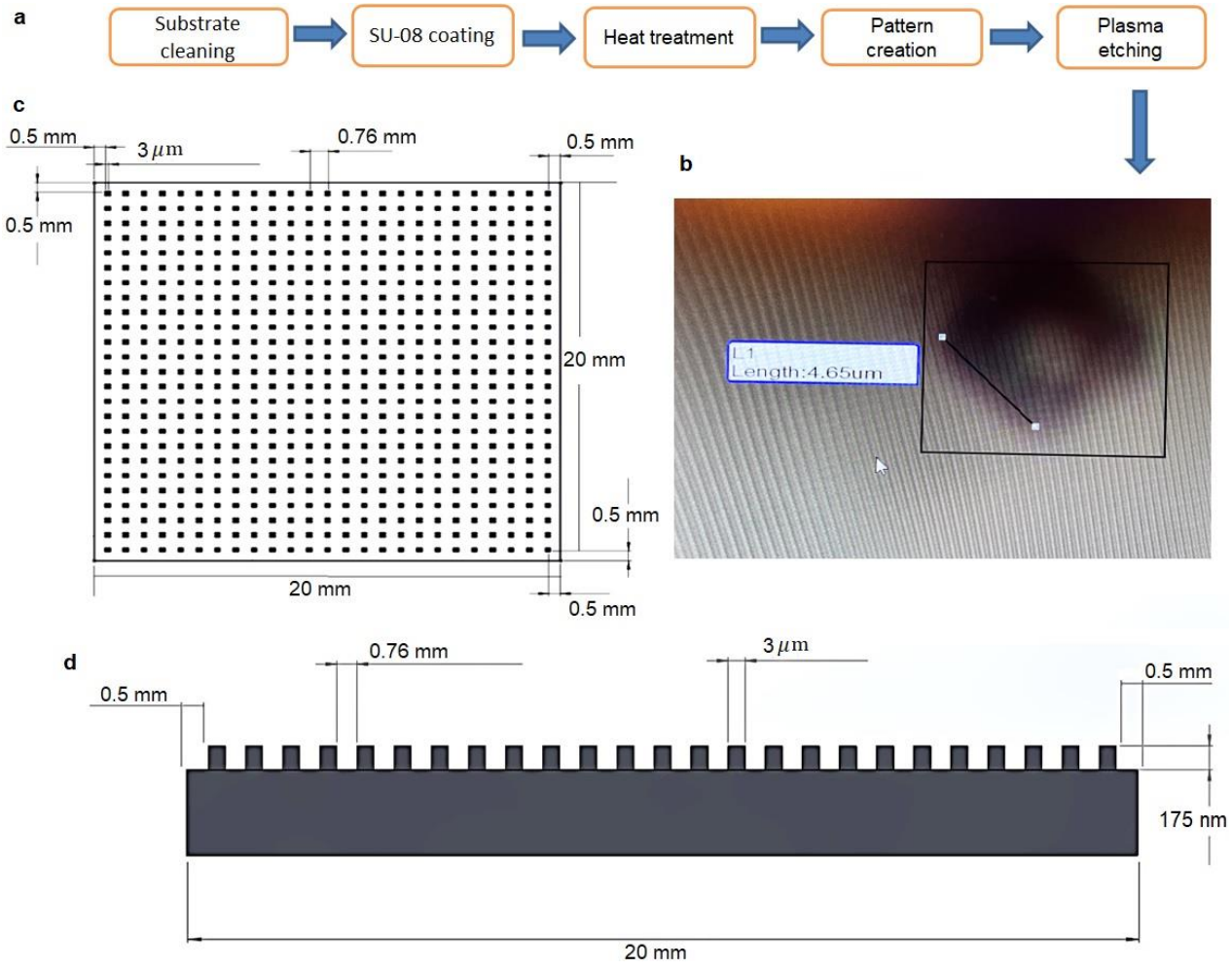

Figure 6.7: (a) SU-8 post fabrication process. (b) SU-8 post on SiC substrate. (c) A schematic top view of SU-8 posts. (d) A schematic side view of the substrate.

After exposure, a post expose bake is performed on a hot plate at 65℃ for 1 minute. The unexposed layer is removed using acetone and the surface is cleaned with isopropanol. Then the substrate is washed with DI water and dried in an oven. The height of the nanopillars can be measured using profilometer and the desired height can be achieved using oxygen plasma etching.

6.2.5 Discussion

We measured the radiative heat transfer for a gap distance of 175 nm between two 15×15 mm^2 SiC plates for temperature difference varying from 15 K up to 70 K. Figure 6.6 shows the measured heat flux. The measured radiative heat flux is 13 times over the blackbody limit. The measured results at a distance of 175 nm match the theoretical predictions obtained using fluctuational electrodynamics. This research demonstrates the near-field radiative heat transfer beyond the far-field blackbody limit. The enhanced radiative heat transfer rate experimentally observed in this study can be useful for energy conversion and thermal management devices that rely on near-field radiative heat transfer.

CHAPTER 7

ENHANCING NEAR-FIELD RADIATIVE HEAT TRANSFER BETWEEN DISSIMILAR DIELECTRIC MEDIA USING GRAPHENE

7.1 Introduction

In the near-field regime, the heat transfer exceeds the far-field blackbody limit by orders of magnitude. The NFRHT between dissimilar dielectric media is not very strong because of the mismatch of their optical properties [63]. Several works have theoretically suggested using graphene to enhance radiative heat flux between dissimilar media. Jihong *et al.,* Song *et al.,* Phan *et al.,* Zhang *et al.,* and Tian *et al.* have theoretically studied the radiative heat transfer between graphene sheets that are either deposited on dielectric substrates or metamaterials, exploring different configurations of surface structure and substrates and their effects [64]–[68]. In addition to being of interest from a fundamental point of view, graphene has been explored for various practical applications including thermophotovoltaic conversion [69], thermal rectification [70], and amplifying heat transfer [51-52]. This study explores the potential of depositing a graphene sheet to enhance near-field radiative heat transfer between dissimilar dielectric media. Graphene consists of a single layer of carbon atoms arranged in a hexagonal lattice, forming a two-dimensional honeycomb structure. Its atomic arrangement gives it exceptional properties like excellent electrical and thermal conductivity, strong mechanical strength, and the ability to transmit light [73]. By using graphene sheets, we aim at achieving enhanced near-field radiative heat transfer rates between dissimilar dielectric materials. We experimentally explore the impact of depositing a graphene's monolayer on a LiF substrate on the near-field radiative heat transfer between LiF and SiC. The results of this research have important applications for improving energy conversion devices and thermal management systems as well as for heat transfer

enhancement. We expect to increase the rate of near-field radiative heat transfer by adding a thin layer of graphene and improve the overall thermal performance of nanoscale devices working based on near-field radiative heat transfer.

7.2 Graphene Transfer Procedure

There are two techniques to transfer graphene from the a Cu foil substrate to LiF substrate, namely standard-based method and direct transfer method [74]. A monolayer graphene sheet on a copper substrate and coated with PMMA was purchased from MSE supply. The thickness of the PMMA layer is usually in the range of 60 – 200 nm. The PMMA layer helps smooth transfer of graphene after Cu etching. Figure 7-1 illustrates the process of transferring graphene from the Cu to LiF substrate.

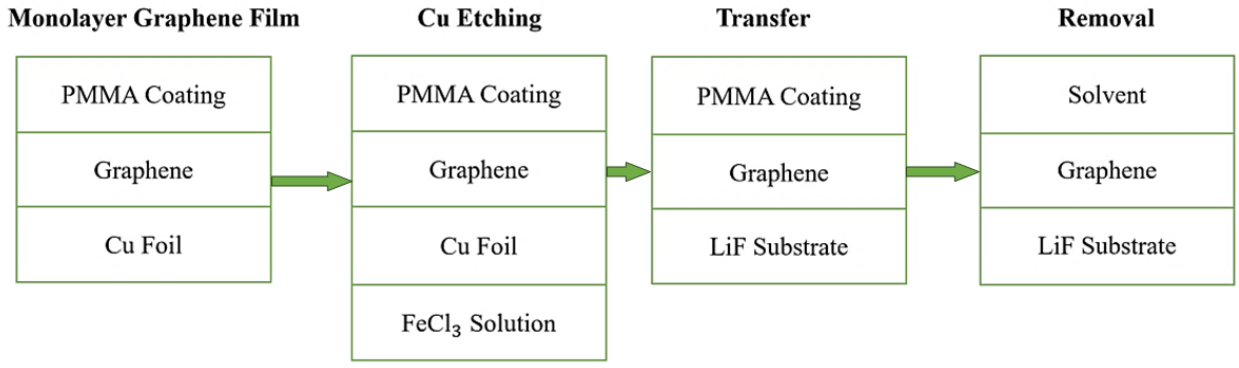

Figure 7.1: Graphene transfer procedure.

We prepared 50% $FeCl_3$ solution with DI water in a beaker. The graphene monolayer on the Cu substrate was placed in the solution, where it floats. The Cu layer was left in the solution for 15 minutes to be etched while the graphene layer with PMMA coating was floating on the solution. The graphene-PMMA then was transferred into DI water slowly to remove the residual solution under the graphene layer. The graphene layer was washed in DI water twice. Then the LiF substrate was placed into the DI water and the graphene was fished from below. We let the sample to dry in

air for 2 hours and then annealed the substrate in a hot chamber at 150℃ for 1 hour. To remove PMMA coating, we used acetone on the layer and then used iso-propyl alcohol. We then baked it for 2 hours at 90℃.

7.3 Numerical Analysis of the Enhancement of Radiative Heat Transfer Between Dissimilar Dielectric Media Using Graphene

We assume a graphene-covered substrate and a bare SiC sample are separated by a vacuum gap of thickness d. Dielectric functions of the LiF and SiC are labelled as, ε_1 and ε_2 respectively. The temperatures of LiF and SiC are T_1 and T_2, respectively. The dielectric functions of both media are modelled using the Drude-Lorentz model as:

$$\varepsilon(\omega) = \varepsilon_\infty \frac{\omega^2 - \omega_{\mathrm{L}}^2 + i\gamma\omega}{\omega^2 - \omega_{\mathrm{T}}^2 + i\gamma\omega} \tag{7-1}$$

Where, ε_∞ is the high-frequency dielectric constant, ω_L and ω_T are the longitudinal and transverse optical phonon frequency respectively, and γ is the damping factor which is a function of purity and material production procedures [75]. We assume the scattering rate is fixed at $\gamma = 8.97 \times 10^{11}$ rad/s for our numerical study [76].

In this section, we theoretically demonstrate significant heat flux enhancement in the presence of a graphene sheet which supports SPPs. The SPPs are emitted in TM-polarization [3]. LiF and SiC can thermally emit SPhPs. However, the spectral locations (i.e., frequencies) of the emitted SPhPs are not the same for these two materials due to dissimilar dielectric properties. This mismatch between the SPhP frequencies of the two materials leads to a substantially small absorption of SPhP modes emitted by the emitter to be absorbed by the receiver, and consequently a small energy transfer occurs.

The Landauer transmission coefficient presented in equation 7-2 are dependent on frequency and wave vector as.

$$T = \begin{cases} \left[\frac{\left(1-|r_{01}^{TE}|^2\right)\left(1-|r_{02}^{TE}|^2\right)}{\left|1-r_{01}^{TE}r_{02}^{TE}e^{2i\,\mathrm{Ro1}(k_{z0})d}\right|^2}+\frac{\left(1-|r_{01}^{TM}|^2\right)\left(1-|r_{02}^{TM}|^2\right)}{\left|1-r_{01}^{TM}r_{02}^{TM}e^{2i\,\mathrm{Ro2}(k_{z0})d}\right|^2}\right], & \boldsymbol{k_\rho} < \frac{\omega}{c}, \\ \left[\frac{\mathrm{Im}\left(r_{01}^{TE}\right)\mathrm{Im}\left(r_{02}^{TE}\right)}{\left|1-r_{01}^{TE}r_{02}^{TE}e^{-2\mathrm{Im}\,(k_{z0})d}\right|^2}+\frac{\mathrm{Im}\left(r_{01}^{TM}\right)\mathrm{Im}\left(r_{02}^{TM}\right)}{|1-r_{01}^{TM}r_{02}^{TM}e^{-2\mathrm{Im}\,(k_{z0})d}|^2}\right], & \boldsymbol{k_\rho} > \frac{\omega}{c}, \end{cases} \quad (7\text{-}2)$$

Here, R_{01} and R_{02} are dependent on the graphene conductivity and a function of the LiF temperature and the chemical potential. We vary the chemical potential between 0 to 1 eV in our analysis. Table 7-1 shows the parameters used in equation 7-1 for modeling the dielectric function of 11 materials. The graphene temperature is assumed as 323 K and the SiC temperature is fixed at 298 K in our numerical analysis.

Table 7-1: The dielectric functions of the substrates used for numerical study of the effect of graphene on heat flux.

Substrate	ω_T (10^{13} rad/s)	ω_L (10^{13} rad/s)	ε_∞ (-)
GaAs [36]	5.1	5.5	11.00
ZnS [36]	5.3	6.6	5.7
GaN [42]	10.53	13.92	5.1
InP [42]	6.80	7.53	9.61
BaF_2 [42]	4.12	4.58	2.16
MgO [42]	5.01	12.56	3.2
SiO_2 [42]	20.04	23.54	2.78
LiF [42]	5.83	12.00	1.9
KCl [42]	2.71	3.96	2.13
KBr [42]	2.18	3.12	2.33
Al_2O_3 [42]	8.80	9.15	16.52

Table 7-2 shows the near-field heat flux between the bare SiC sample and graphene coated substrate for the 11 substrates listed in Table 7-1. Table 7-2 helps to determine the substrate that offers a substantial heat flux for the near-field radiative heat transfer experiment in the presence of a graphene sheet. The emitting substrate, heated using the ceramic heater, is kept at a temperature of T_1 = 323 K, while the receiving SiC substrate, which is cooled down using a TEC, is kept at T_2 = 298 K. The distance between two plates, d, is equal to the height of SU-8 nano pillars, i.e., d = 175 nm.

Table 7-2: Radiative heat transfer analysis between dissimilar dielectric media.

Emitter material (T_1) - SiC (T_2)	Heat Flux (Wm^{-2}) No Graphene	Max Heat Flux (Wm^{-2}) With Graphene	Graphene Chemical Potential
GaAs - SiC	749	758	1
ZnS - SiC	532	682	0.96
GaN - SiC	557	910	1
InP - SiC	670	689	1
BaF_2 - SiC	254	677	0.62
MgO - SiC	240	705	0.56
SiO_2 - SiC	319	378	1
LiF - SiC	186	706	0.43
KCl - SiC	242	670	0.62
KBr - SiC	277	686	0.68
Al_2O_3 - SiC	817	819	0

Figure 7-2 shows the simulated total radiative heat flux for a chemical potential of graphene which results in the largest heat flux. The numerical results show that the presence of graphene can change the heat flux significantly. The highest heat transfer for LiF and SiC occurs when the chemical potential is equal to 0.43.

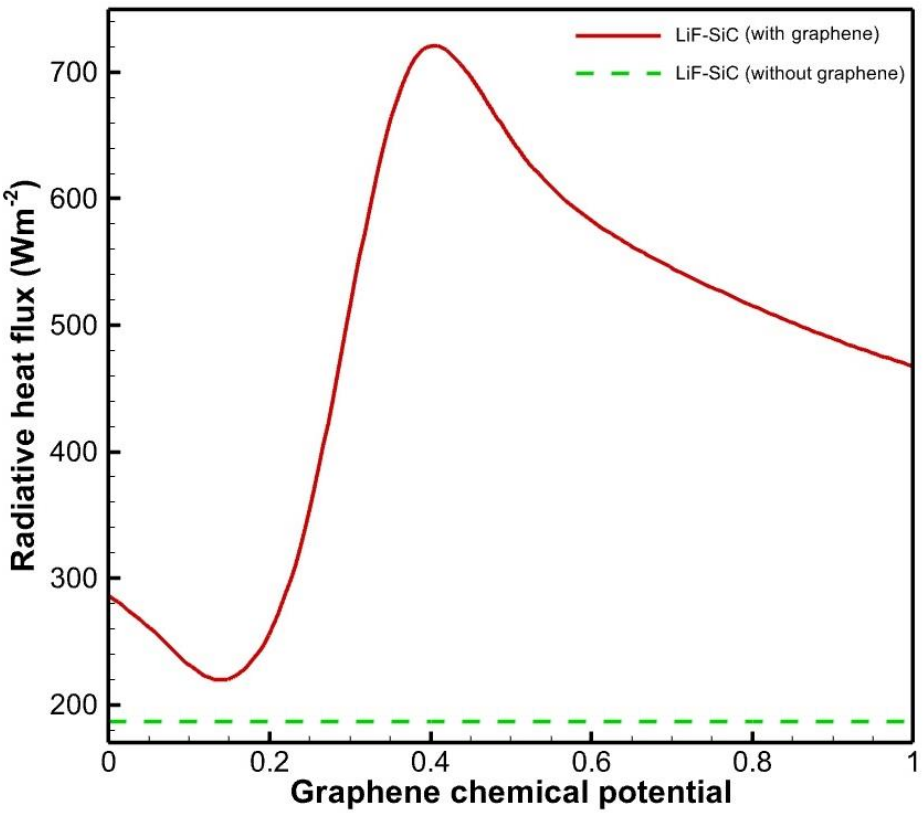

Figure 7.2: The radiative heat flux versus the graphene chemical potential. The solid line represents the heat flux between LiF and SiC in the presence of the graphene sheet on the LiF substrate, while the dashed line shows the radiative heat flux between LiF and SiC without a graphene layer. The LiF temperature is at 323 K and the SiC is at 298 K. The LiF and SiC are separated by a 175 nm gap.

7.4 Heat Flux Measurement

The system considered for the radiative heat transfer analysis consists of two parallel planar slabs. We consider LiF as the first slab which is attached to the heater and SiC as the second slab which is kept at 293 K and attached to a TEC. The gap between the two materials is 175 nm. We inititially measured NFRHT between LiF and SiC without any graphene layer. Then we measured the heat flux in the presence of a graphene layer on LiF. The measured and simulated heat flux are shown in Figure 7-3. The vacuum pressure in the chamber was $1.77 \times 10^{-7} - 7.58 \times 10^{-8}$ Torr for several measurement trials.

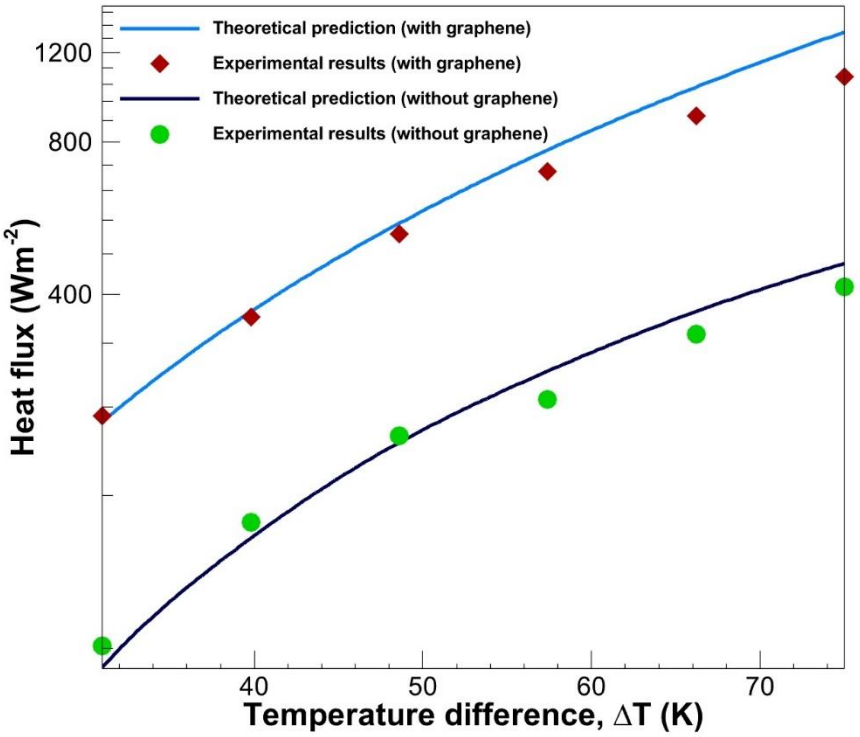

Figure 7.3: Radiative heat flux between LiF and SiC plates in the absence of graphene and with a graphene monolayer.

7.5 Discussion

The spectral heat flux between SiC – SiC, LiF – LiF, and LiF – SiC is shown in Figure 7-4. The temperatures of the hot and cold sides are assumed as 393 K and 293 K, respectively, and the separation gap is fixed at 175 nm. There is a sharp peak in the heat flux spectrum for SiC – SiC and LiF – LiF cases at 1.02×10^{14} rad/s and 1.79×10^{14} rad/s, respectively, which are due to thermal emission and absorption of the surface phonon polaritons (SPhPs) by these two materials. Surface phonon polaritons are excited due to the coupling of the electromagnetic waves with the transverse optical phonons (mechanical vibrations of ions) in the dielectric media. They are evanescent waves in both the dielectric medium and the free space and propagate parallel to the interface. The thermal excitation of the SPhPs resonantly increases the heat flux at a frequency for which the $\mathrm{Re}[\varepsilon] \approx -1$, where ε is the dielectric function of the material. Since the dielectric function of the SiC and LiF are different, the frequencies at which SPhP modes are excited are different for these two materials.

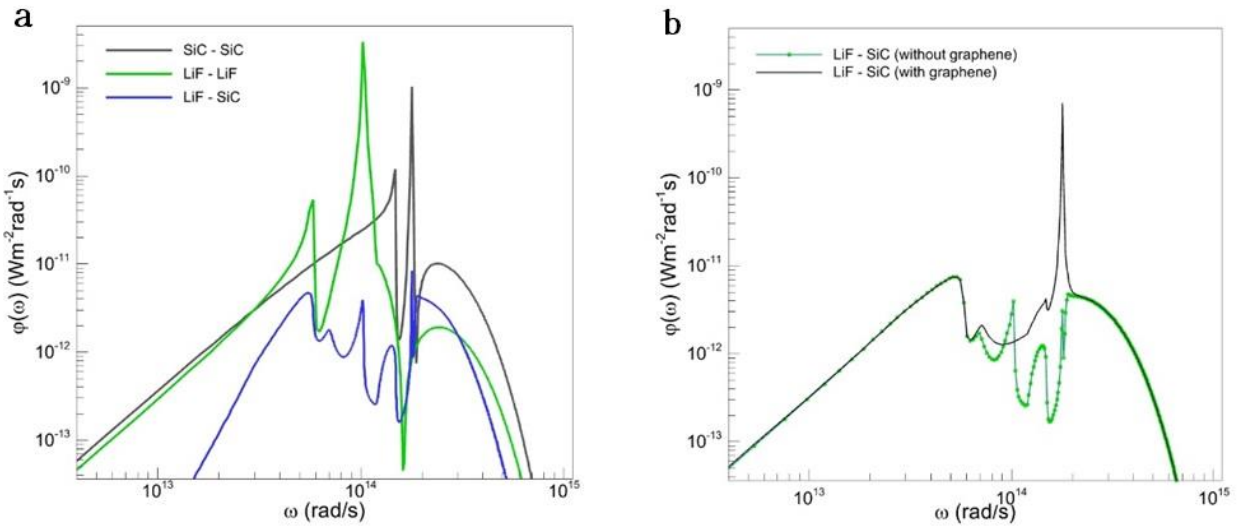

Figure 7.4: Spectral heat flux $\varphi(\omega)$ between two semi-infinite planar media separated by a vacuum gap of size d = 175. The hot side temperature is 393 K, while the cold side is assumed at 293 K.

(a) The heat flux between three configurations of similar dielectric media, namely SiC – SiC (black curve), LiF – LiF (green curve), and LiF – SiC (blue curve), in the absence of a graphene sheet. (b) The spectral heat flux between two dissimilar dielectric media (LiF – SiC) in the absence of graphene and in the presence of a graphene monolayer on LiF.

The Landauer transmission function for emitted electromagnetic waves with a frequency ω and a wavevector k_ρ is plotted in Figures 7-5a and 7-5b for LiF – LiF and SiC – SiC cases, respectively. The Landauer transmission function is plotted for electromagnetic waves which have a transverse magnetic ™ polarization as the near-field heat flux is dominated by contribution of these modes. The Landauer transmission function shows the probability that a given electromagnetic wave, characterized by its frequency and wavevector (ω, k_ρ), is emitted by one medium and is absorbed by the second medium. As it is seen from these two figures, there is a region with large value of transmission function which is due to the contribution from SPhPs. While LiF and SiC both support SPhPs, the transmission function for the SiC – LiF, which is also shown in Fig. 7-5c, is much smaller than that for SiC – SiC and LiF – LiF cases. The reason for the small transmission function for the SiC-LiF case can be explained as follows:

Based on Kirchhoff's law, a material is a good absorber of thermal radiation at the frequency for which is highly emits. As such, for the cases of similar dielectrics, thermal radiation of the SPhPs from the emitting medium is highly absorbed by the receiving medium resulting in a resonant heat flux. However, for the case of dissimilar dielectric media, while the emitting medium radiates SPhP modes, these modes cannot be efficiently absorbed by the receiving medium resulting in a lower heat flux value.

The transmission function for LiF – SiC case is shown in Figure 7-5c. As it is seen from this figure, even though both LiF and SiC thermally emit SPhPs modes, these modes do not efficiently transfer heat as the emission frequency of the SPhP modes is not the same as a frequency with high absorption for the receiver. Figure 7-4b shows the spectral heat flux for SiC – LiF case when a graphene sheet is deposited on the LiF substrate. It is seen that the heat flux has a very sharp peak at 1.79×10^{14} rad/s. It should be noted that the y-axis in Fig. 7-4b is in logarithmic scale, showing that the heat flux at the peak frequency is at least 100 orders of magnitude greater than at other frequencies (i.e., heat flux is quasi-monochromatic).

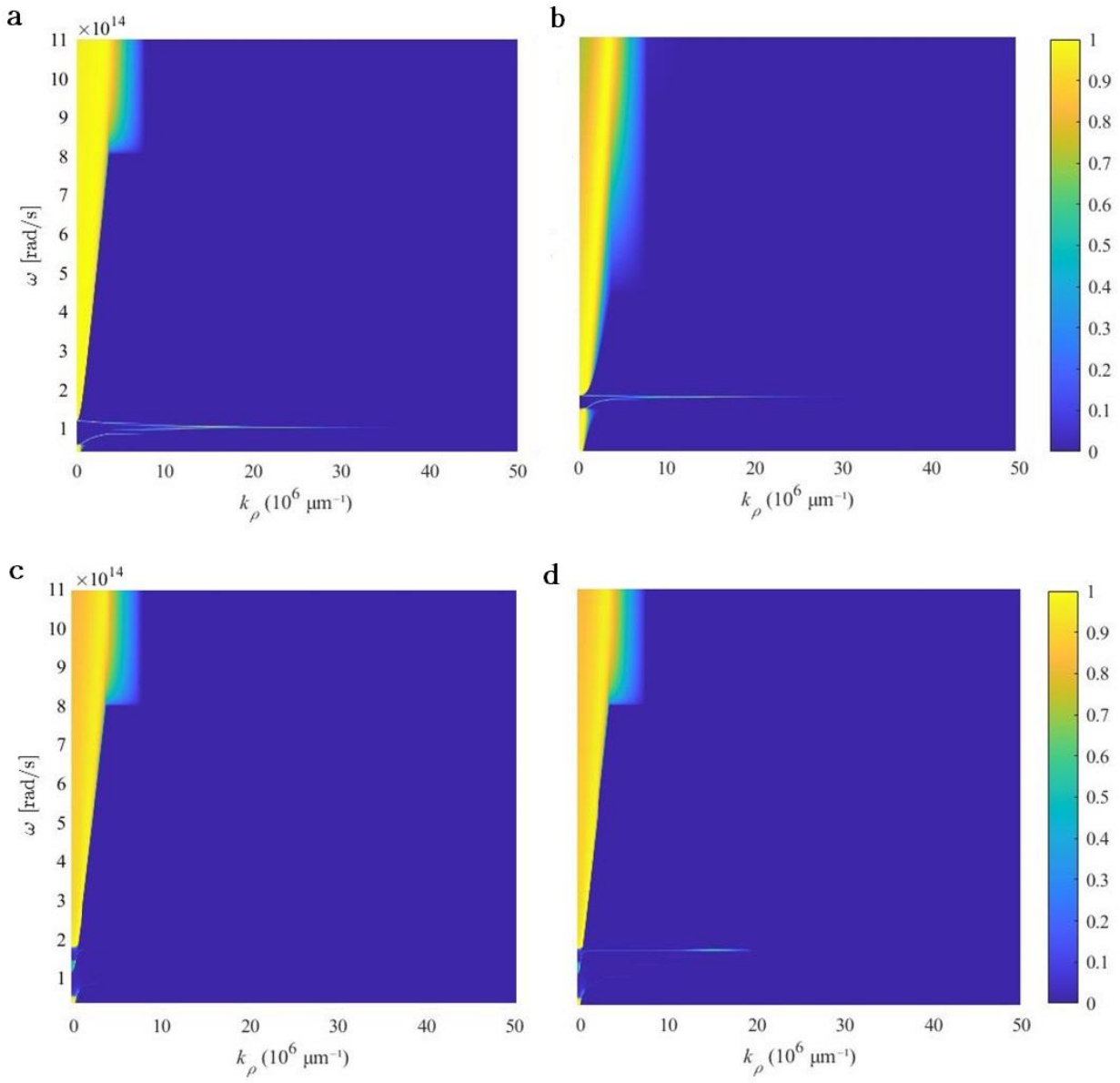

Figure 7.5: Landauer transmission function $\zeta_\rho(\omega, \mathrm{k})$ for two planar media at 293 K and 393 K separated by a vacuum gap of size d = 175 nm. The transmission function is plotted in the (k_ρ, ω) plane for the TM-polarized electromagnetic waves. (a) LiF – LiF without graphene. (b) SiC – SiC without graphene. (c) SiC – LiF without graphene. (d) SiC – LiF with graphene.

The appearance of this peak is due to the coupling of the surface plasmon polaritons (SPPs) emitted by the graphene sheet to the SPhP modes of LiF which modified the dispersion of the surface mode to peak at a frequency for which SPhPs of the SiC exist. The appearance of the coupled SPP-SPhP modes can be seen from Fig. 7-5d which shows the transmission function for the SiC – LiF in the presence of graphene. The appearance of this peak increases the heat flux relative to the case without a graphene sheet by 250 – 290 %.

CHAPTER 8

CONCLUSION

Near-field radiative heat transfer (NFRHT) between similar and dissimilar dielectric media is studied both theoretically and experimentally. We developed an experimental setup for analyzing radiative heat transfer both in near-field and far-field. We used blackbody, quartz, SiC and LiF substrates in our experimental analysis. Experimental results of near-field radiative heat transfer between quartz plates separated by gap distances of 100 nm and 200 nm show an enhanced heat flux compared to the far-field regime. However, the measured near-field heat fluxes do not match the theoretical predictions due to non-uniform deposition of polystyrene particles. We then adopt another technique for establishing a uniform vacuum gap distance between two planar surfaces, i.e., by using SU-8 nano-pillars. The experimental gap distance between two surfaces is 175 nm for SiC – SiC and LiF – SiC experiments. In chapter 7, our experiments with graphene layer on LiF show that radiative heat transfer in near-field regime can be amplified by using graphene on one of the surfaces. The coupling of the surface plasmon polaritons of graphene with the surface phonon polaritons of the LiF changes the dispersion relation of the surface modes such that the emitted surface modes can be absorbed by the receiver more effectively. The theoretical study of the near-field radiative heat transfer between dissimilar dielectric media in the presence of a graphene sheet is done using fluctuational electrodynamics.

The experimental setup demonstrated in this study can be modified in future experiments to control the gap distance between two planar surfaces. In addition, we can extend our work by considering amplification of heat transfer between similar dielectric materials by using a graphene sheet. We can also use thin films coating of metal on a substrate to investigate the effects of coupling of SPPs of metals with the SPPs of the graphene sheet on the near field radiative heat transfer. Our

experimental investigations are validated by theoretical simulations. However, the accuracy of experiments can be enhanced further by analyzing the parallelism of the two flat plates. Our assumption in numerical study is that the surface roughness is almost zero. In practical cases, the surface roughness could alter the experimental results.

To summarize, we experimentally showed the enhancement of radiative heat transfer in the near-field regime over the blackbody limit. We experimentally demonstrated that near-field radiative heat transfer between dissimilar dielectric media can be enhanced by depositing a graphene layer on one of the dielectric media. We theoretically showed that this enhancement is due to the modification of the dispersion relation of surface phonon polaritons of the dielectric media in the presence of the graphene layer.

REFERENCES

[1] M. Planck, *The theory of heat radiation*. New York: Dover Publications, 1991.

[2] E. Hecht, *Optics*, 5 ed. Boston: Pearson Education, Inc, 2017.

[3] K. Joulain, J.-P. Mulet, F. Marquier, R. Carminati, and J.-J. Greffet, "Surface electromagnetic waves thermally excited: Radiative heat transfer, coherence properties and Casimir forces revisited in the near field," *Surf. Sci. Rep.*, vol. 57, no. 3–4, pp. 59–112, May 2005.

[4] M. F. Modest, *Radiative heat transfer*, Third Edition. New York: Academic Press, 2013.

[5] L. Tsang, J. A. Kong, and K.-H. Ding, *Scattering of Electromagnetic Waves: Theories and Applications*. New York, USA: John Wiley & Sons, Inc., 2000.

[6] S. M. Rytov, *Principles of statistical radiophysics 3: elements of random fields*. Place of publication not identified: Springer, 2012.

[7] "Fossil Fuels." https://www.eesi.org/topics/fossil-fuels/description#:~:text=Fossil%20fuels%E2%80%94including%20coal%2C%20oil,percent%20of%20the%20world's%20energy.

[8] C. Jiang, H. Huang, and Z. Zhou, "Enhancement in the multi-junction thermophotovoltaic system based on near-field heat transfer and hyperbolic metamaterial," *Sol. Energy*, vol. 217, pp. 390–398, Mar. 2021.

[9] R. Mittapally *et al.*, "Near-field thermophotovoltaics for efficient heat to electricity conversion at high power density," *Nat. Commun.*, vol. 12, no. 1, p. 4364, Jul. 2021.

[10] G. R. Bhatt *et al.*, "Integrated near-field thermo-photovoltaics for heat recycling," *Nat. Commun.*, vol. 11, no. 1, p. 2545, May 2020.

[11] L. Hu, A. Narayanaswamy, X. Chen, and G. Chen, "Near-field thermal radiation between two closely spaced glass plates exceeding Planck's blackbody radiation law," *Appl. Phys. Lett.*, vol. 92, no. 13, p. 133106, Mar. 2008.

[12] T. Ijiro and N. Yamada, "Near-field radiative heat transfer between two parallel SiO_2 plates with and without microcavities," *Appl. Phys. Lett.*, vol. 106, no. 2, p. 023103, Jan. 2015.

[13] P. Sabbaghi *et al.*, "Super-Planckian radiative heat transfer between macroscale metallic surfaces due to near-field and thin-film effects," *J. Appl. Phys.*, vol. 128, no. 2, p. 025305, Jul. 2020.

[14] N. H. Thomas, M. C. Sherrott, J. Broulliet, H. A. Atwater, and A. J. Minnich, “Electronic Modulation of Near-Field Radiative Transfer in Graphene Field Effect Heterostructures,” *Nano Lett.*, vol. 19, no. 6, pp. 3898–3904, Jun. 2019.

[15] C. M. Hargreaves, “Anomalous radiative transfer between closely-spaced bodies,” *Phys. Lett. A*, vol. 30, no. 9, pp. 491–492, Dec. 1969, doi: 10.1016/0375-9601(69)90264-3.

[16] D. Polder and M. Van Hove, “Theory of Radiative Heat Transfer between Closely Spaced Bodies,” *Phys. Rev. B*, vol. 4, no. 10, pp. 3303–3314, Nov. 1971.

[17] B. Guha, C. Otey, C. B. Poitras, S. Fan, and M. Lipson, “Near-Field Radiative Cooling of Nanostructures,” *Nano Lett.*, vol. 12, no. 9, pp. 4546–4550, Sep. 2012.

[18] F. Chen, X. Liu, Y. Tian, and Y. Zheng, “Dynamic Tuning of Near-field Radiative Thermal Rectification,” 2020.

[19] H. Iizuka and S. Fan, “Rectification of evanescent heat transfer between dielectric-coated and uncoated silicon carbide plates,” *J. Appl. Phys.*, vol. 112, no. 2, p. 024304, Jul. 2012.

[20] L. Zhu, A. Fiorino, D. Thompson, R. Mittapally, E. Meyhofer, and P. Reddy, “Near-field photonic cooling through control of the chemical potential of photons,” *Nature*, vol. 566, no. 7743, pp. 239–244, Feb. 2019.

[21] B. Zhao, P. Santhanam, K. Chen, S. Buddhiraju, and S. Fan, “Near-Field Thermophotonic Systems for Low-Grade Waste-Heat Recovery,” *Nano Lett.*, vol. 18, no. 8, pp. 5224–5230, Aug. 2018.

[22] W. A. Challener *et al.*, “Heat-assisted magnetic recording by a near-field transducer with efficient optical energy transfer,” *Nat. Photonics*, vol. 3, no. 4, pp. 220–224, Apr. 2009.

[23] N. Zhou *et al.*, “Plasmonic near-field transducer for heat-assisted magnetic recording,” *Nanophotonics*, vol. 3, no. 3, pp. 141–155, Jun. 2014.

[24] W. A. Challener and A. V. Itagi, “Near-Field Optics for Heat-Assisted Magnetic Recording (Experiment, Theory, and Modeling),” in *Modern Aspects of Electrochemistry No. 44*, M. Schlesinger, Ed., in Modern Aspects of Electrochemistry, vol. 44. New York, NY: Springer New York, 2009, pp. 53–111.

[25] K. Joulain, P. Ben-Abdallah, P.-O. Chapuis, Y. De Wilde, A. Babuty, and C. Henkel, “Strong tip–sample coupling in thermal radiation scanning tunneling microscopy,” *J. Quant. Spectrosc. Radiat. Transf.*, vol. 136, pp. 1–15, Mar. 2014.

[26] A. N. Grigorenko, M. Polini, and K. S. Novoselov, “Graphene plasmonics,” *Nat. Photonics*, vol. 6, no. 11, pp. 749–758, Nov. 2012.

[27] C. Guo *et al.*, “Graphene-Based Perfect Absorption Structures in the Visible to Terahertz Band and Their Optoelectronics Applications,” *Nanomaterials*, vol. 8, no. 12, p. 1033, Dec. 2018.

[28] V. B. Svetovoy and G. Palasantzas, “Graphene-on-Silicon Near-Field Thermophotovoltaic Cell,” *Phys. Rev. Appl.*, vol. 2, no. 3, p. 034006, Sep. 2014.

[29] J. Yang *et al.*, “Observing of the super-Planckian near-field thermal radiation between graphene sheets,” *Nat. Commun.*, vol. 9, no. 1, p. 4033, Oct. 2018.

[30] R. Messina and P. Ben-Abdallah, “Graphene-based photovoltaic cells for near-field thermal energy conversion,” *Sci. Rep.*, vol. 3, no. 1, p. 1383, Mar. 2013, doi: 10.1038/srep01383.

[31] M. D. Whale and E. G. Cravalho, “Modeling and performance of microscale thermophotovoltaic energy conversion devices,” *IEEE Trans. Energy Convers.*, vol. 17, no. 1, pp. 130–142, Mar. 2002.

[32] B. Xu, Z. Cen, Y. T. Toh, J. Li, K. Ye, and J. Zhang, “Efficiency Analysis of Near Field Optical Transducer Used in Heat-Assisted Magnetic Recording,” *IEEE Trans. Magn.*, vol. 49, no. 7, pp. 3580–3583, Jul. 2013.

[33] A. Datta and X. Xu, “Optical and thermal designs of near field transducer for heat assisted magnetic recording,” *Jpn. J. Appl. Phys.*, vol. 57, no. 9S2, p. 09TA01, Sep. 2018.

[34] J. DeSutter, L. Tang, and M. Francoeur, “A near-field radiative heat transfer device,” *Nat. Nanotechnol.*, vol. 14, no. 8, pp. 751–755, Aug. 2019.

[35] J. I. Watjen, B. Zhao, and Z. M. Zhang, “Near-field radiative heat transfer between doped-Si parallel plates separated by a spacing down to 200 nm,” *Appl. Phys. Lett.*, vol. 109, no. 20, p. 203112, Nov. 2016.

[36] R. Messina, P. Ben-Abdallah, B. Guizal, and M. Antezza, “Graphene-based amplification and tuning of near-field radiative heat transfer between dissimilar polar materials,” *Phys. Rev. B*, vol. 96, no. 4, p. 045402, Jul. 2017.

[37] “Wien’s law illustrated.” https://www.physics.unlv.edu/~jeffery/astro/blackbody/wien_law.html.

[38] “Climate Science Investigations.,” May 10, 2023. http://www.ces.fau.edu/ nasa/module-2/radiation-sun.php.

[39] Z. M. Zhang, *Nano/microscale heat transfer*, Second edition. in Mechanical engineering series. Cham, Switzerland: Springer, 2020.

[40] B. Z. Tajani, “The Effect of Non-Local Electrical Conductivity on Near-Field Radiative Heat Transfer Between Graphene Sheets,” 2021. [Online]. Available: https://digitalcommons.library.umaine.edu/etd/3471

[41] C. Altman and K. Suchy, *Reciprocity, spatial mapping and time reversal in electromagnetics*. in Developments in electromagnetic theory and applications, no. v. 9. Dordrecht ; Boston: Kluwer Academic Publishers, 1991.

[42] M. Habibzadeh, H. Lin, and S. Edalatpour, “Near-field radiative heat transfer between on-substrate graphene sheets,” *J. Quant. Spectrosc. Radiat. Transf.*, vol. 307, p. 108662, Oct. 2023.

[43] S. Zare, B. Zeinali Tajani, and S. Edalatpour, “Effect of nonlocal electrical conductivity on near-field radiative heat transfer between graphene sheets,” *Phys. Rev. B*, vol. 105, no. 12, p. 125416, Mar. 2022.

[44] S. A. Maier, *Plasmonics: fundamentals and applications*. New York: Springer, 2007.

[45] H. Raether, *Surface Plasmons on Smooth and Rough Surfaces and on Gratings*. in Springer Tracts in Modern Physics, no. 111. Berlin, Heidelberg: Springer-Verlag Springer e-books, 1988.

[46] S. Basu, Y.-B. Chen, and Z. M. Zhang, “Microscale radiation in thermophotovoltaic devices—A review,” *Int. J. Energy Res.*, vol. 31, no. 6–7, pp. 689–716, May 2007.

[47] A. Narayanaswamy and G. Chen, “Surface modes for near field thermophotovoltaics,” *Appl. Phys. Lett.*, vol. 82, no. 20, pp. 3544–3546, May 2003.

[48] M. Laroche, R. Carminati, and J.-J. Greffet, “Near-field thermophotovoltaic energy conversion,” *J. Appl. Phys.*, vol. 100, no. 6, p. 063704, Sep. 2006.

[49] R. S. Ottens *et al.*, “Near-Field Radiative Heat Transfer between Macroscopic Planar Surfaces,” *Phys. Rev. Lett.*, vol. 107, no. 1, p. 014301, Jun. 2011.

[50] T. Kralik, P. Hanzelka, V. Musilova, A. Srnka, and M. Zobac, “Cryogenic apparatus for study of near-field heat transfer,” *Rev. Sci. Instrum.*, vol. 82, no. 5, p. 055106, May 2011.

[51] T. Kralik, P. Hanzelka, M. Zobac, V. Musilova, T. Fort, and M. Horak, “Strong Near-Field Enhancement of Radiative Heat Transfer between Metallic Surfaces,” *Phys. Rev. Lett.*, vol. 109, no. 22, p. 224302, Nov. 2012.

[52] M. Ghashami, H. Geng, T. Kim, N. Iacopino, S. K. Cho, and K. Park, “Precision Measurement of Phonon-Polaritonic Near-Field Energy Transfer between Macroscale Planar Structures Under Large Thermal Gradients,” *Phys. Rev. Lett.*, vol. 120, no. 17, p. 175901, Apr. 2018.

[53] B. Song, D. Thompson, A. Fiorino, Y. Ganjeh, P. Reddy, and E. Meyhofer, “Radiative heat conductances between dielectric and metallic parallel plates with nanoscale gaps,” *Nat. Nanotechnol.*, vol. 11, no. 6, pp. 509–514, Jun. 2016.

[54] K. Ito, A. Miura, H. Iizuka, and H. Toshiyoshi, “Parallel-plate submicron gap formed by micromachined low-density pillars for near-field radiative heat transfer,” *Appl. Phys. Lett.*, vol. 106, no. 8, p. 083504, Feb. 2015.

[55] M. P. Bernardi, D. Milovich, and M. Francoeur, “Radiative heat transfer exceeding the blackbody limit between macroscale planar surfaces separated by a nanosize vacuum gap,” *Nat. Commun.*, vol. 7, no. 1, p. 12900, Sep. 2016.

[56] X. Ying, P. Sabbaghi, N. Sluder, and L. Wang, “Super-Planckian Radiative Heat Transfer between Macroscale Surfaces with Vacuum Gaps Down to 190 nm Directly Created by SU-8 Posts and Characterized by Capacitance Method,” *ACS Photonics*, vol. 7, no. 1, pp. 190–196, Jan. 2020.

[57] R. Teja, “Arduino Mega Pinout | Arduino Mega 2560 Layout, Specifications.” https://www.electronicshub.org/arduino-mega-pinout/.

[58] “MAX31856 Breakout - Universal Thermocouple Amplifier - Adafruit 3263.” https://botland.store/accessories-for-temperature-sensors/7682-max31856-breakout-universal-thermocouple-amplifier-adafruit-3263-5904422336066.html.

[59] F. P. Incropera, D. P. DeWitt, T. L. Bergman, and A. S. Lavine, Eds., *Fundamentals of heat and mass transfer*, 6th ed. Hoboken, NJ: John Wiley & Sons, 2006.

[60] “CORK INSULATION FAQS.” https://thermalcorksolutions.com/cork-insulation-faqs/#:~:text=The%20thermal%20conductivity%20of%20cork,cope%20with%20significant%20thermal%20variations.

[61] “Non-Functionalized Colloidal Polystyrene Nanospheres.” https://www.alphananotechne.com/polystyrene-nanoparticles.

[62] R.-C. Voicu, M. A. Zandi, R. Müller, and C. Wang, “Nonlinear numerical analysis and experimental testing for an electrothermal SU-8 microgripper with reduced out-of-plane displacement,” *J. Phys. Conf. Ser.*, vol. 922, p. 012006, Nov. 2017.

[63] P. Ben-Abdallah and K. Joulain, “Fundamental limits for noncontact transfers between two bodies,” *Phys. Rev. B*, vol. 82, no. 12, p. 121419, Sep. 2010.

[64] X. Liu, R. Z. Zhang, and Z. Zhang, “Near-Perfect Photon Tunneling by Hybridizing Graphene Plasmons and Hyperbolic Modes,” *ACS Photonics*, vol. 1, no. 9, pp. 785–789, Sep. 2014.

[65] D. Drosdoff, A. D. Phan, and L. M. Woods, “Transverse Electric Mode for Near-Field Radiative Heat Transfer in Graphene-Metamaterial Systems,” *Adv. Opt. Mater.*, vol. 2, no. 11, pp. 1038–1042, Nov. 2014.

[66] R. Z. Zhang, X. Liu, and Z. M. Zhang, “Near-field radiation between graphene-covered carbon nanotube arrays,” *AIP Adv.*, vol. 5, no. 5, p. 053501, May 2015.

[67] J.-Y. Chang, Y. Yang, and L. Wang, “Enhanced energy transfer by near-field coupling of a nanostructured metamaterial with a graphene-covered plate,” *J. Quant. Spectrosc. Radiat. Transf.*, vol. 184, pp. 58–67, Nov. 2016.

[68] J. Song and Q. Cheng, “Near-field radiative heat transfer between graphene and anisotropic magneto-dielectric hyperbolic metamaterials,” *Phys. Rev. B*, vol. 94, no. 12, p. 125419, Sep. 2016.

[69] O. Ilic, M. Jablan, J. D. Joannopoulos, I. Celanovic, and M. Soljačić, “Overcoming the black body limit in plasmonic and graphene near-field thermophotovoltaic systems,” *Opt. Express*, vol. 20, no. S3, p. A366, May 2012.

[70] Z. Zheng, X. Liu, A. Wang, and Y. Xuan, “Graphene-assisted near-field radiative thermal rectifier based on phase transition of vanadium dioxide (VO2),” *Int. J. Heat Mass Transf.*, vol. 109, pp. 63–72, Jun. 2017.

[71] K. Shi, F. Bao, and S. He, “Enhanced Near-Field Thermal Radiation Based on Multilayer Graphene-hBN Heterostructures,” *ACS Photonics*, vol. 4, no. 4, pp. 971–978, Apr. 2017.

[72] L.-Y. Zhong, Q.-M. Zhao, T.-B. Wang, T.-B. Yu, Q.-H. Liao, and N.-H. Liu, “Near-Field Radiative Heat Transfer Between Graphene/Silicon Carbide Multilayers,” *J. Heat Transf.*, vol. 140, no. 7, p. 072701, Jul. 2018.

[73] V. B. Mbayachi, E. Ndayiragije, T. Sammani, S. Taj, E. R. Mbuta, and A. U. Khan, “Graphene synthesis, characterization and its applications: A review,” *Results Chem.*, vol. 3, p. 100163, Jan. 2021.

[74] W. Regan *et al.*, “A direct transfer of layer-area graphene,” *Appl. Phys. Lett.*, vol. 96, no. 11, p. 113102, Mar. 2010.

[75] E. D. Palik, *Handbook of optical constants of solids. III*. San Diego: Academic Press, 1998.

[76] Y. Yang and L. Wang, “Electrically-controlled near-field radiative thermal modulator made of graphene-coated silicon carbide plates,” *J. Quant. Spectrosc. Radiat. Transf.*, vol. 197, pp. 68–75, Aug. 2017.

BIOGRAPHY OF THE AUTHOR

Md Shofiqul Islam was born in Chittagong, Bangladesh on June 07, 1992. He was raised in Chittagong and graduated from Chittagong College in 2011. He attended Chittagong University of Engineering and Technology and graduated in 2017 with a Bachelor's degree in Mechanical Engineering. He also worked as a Mechanical Engineer for several years from 2017 to 2019. Later, he joined the Department of Mechanical Engineering at the University of Maine in August 2021. Md Shofiqul Islam is a candidate for the Master of Science degree in Mechanical Engineering from the University of Maine in December 2023.